RESEARCH

The Possible Role of Anoxic Alkaline High Subcritical Water in the Formation of Ferric Minerals, Methane and Disordered Graphitic Carbon in a BARB3 Drilled Sample of the 3.4 Ga Buck Reef Chert

Marie-Paule Bassez[1] (ORCID)

Abstract

The present article reports Raman spectroscopic observations of siderite, hematite, disordered graphitic carbon and possibly greenalite inside the quartz matrix of a banded iron sample from the BARB3 core drilled inside the 3.4 Ga Buck Reef Chert of the Barberton Greenstone Belt in South Africa. The article also reports Raman spectroscopic observations of quartz cavities, concluding in the presence of water, methane and sodium hydroxide at high concentration leading to pH ~ 15 inside the inclusion, suggesting an Archean water which was strongly basic. Fe^{III}-greenalite may also be present inside the inclusion. The possible role of anoxic alkaline high subcritical water in the formation of ferric minerals and the CO required for the synthesis of molecules of biological interest has been demonstrated theoretically since 2013 and summarized in the concept of Geobiotropy. The present article experimentally confirms the importance of considering water in its anoxic strongly alkaline high subcritical domain for the formation of quartz, hematite, Fe^{III}-greenalite, methane and disordered graphitic carbon. Methane is proposed to form locally when the carbon dioxide that is dissolved in the Archean anoxic alkaline high subcritical water, interacts with the molecular hydrogen that is emitted during the anoxic alkaline oxidation of ferrous silicates. The carbon matter is proposed to form as deposition from the anoxic methane-rich fluid. A detailed study of carbon matter from diverse origins is presented in a supplementary file. The study shows that the BARB3_23B sample has been submitted to ~ 335 °C, a temperature of the high subcritical domain, and that the graphitic structure contains very low amounts of oxygen and no hydroxyl functional groups. The importance of considering the structure of water is applied to the constructions of the Neoproterozoic and Archean banded iron formations. It is proposed that their minerals are produced inside chemical reaction chambers containing ferrous silicates, and ejected from the Earth's oceanic crust or upper mantle, during processes involving subduction events or not.

Keyword BIFs · NIFs · BARB3 · Buck Reef Chert · Geobiotropy · Archean ferric minerals

✉ Marie-Paule Bassez
   marie-paule.bassez@unistra.fr

1   University of Strasbourg, Jean-Marie Lehn Foundation, Strasbourg, France

Introduction

The presence of ferric iron inside rocks is explained by the oxidation of ferrous iron with oxygen, or by the reduction of water in the presence of UV light at acidic pH 1 to 3 as described in (Cairns-Smith 1978). Up to now it is accepted that in anoxic environments such as terrestrial Archean times, ferrous iron is oxidized by microorganisms who produce oxygen or directly oxidize Fe^{2+}. Oxidation by microorganisms is at the present time the explanation for the presence of ferric iron in Banded Iron Formations, as introduced in (Bassez 2019a and refs therein) and recently studied in (Wang et al. 2023; Schad et al. 2022; Kiyokawa et al. 2020). Ferric iron minerals under the form of Fe_2O_3 are also reported in the deeper crust and even in the upper mantle (Frost 2022). In the past fifty years, hydrogen gas associated with ferric minerals and alkaline spring water (pH > 12) has been observed emerging from ultramafic rocks such as the margins of oceanic spreading centres, oceanic transform faults, subduction zones (Neal and Stanger 1983, and refs therein).

Trying to understand the origin of H_2 I conducted research on the structure of supercritical water (Bassez 1998) and high-pressure water (Bassez 2003), and on the relation between the structure of water and prebiotic chemistry (Bassez 2003, 2008a, b, 2009). In 2012 was published an article showing redox Pourbaix diagrams for the system Fe-H_2O in high subcritical water conditions (Cook and Olive 2012). Studying this diagram I noticed that at strongly basic pH, water at 300°-350 °C, 10–25 MPa can oxidize Fe^{2+}. Envisioning that this path of oxidation might explain many geological sites on Earth and rocky objects in the Universe, I developed a model named Geobiotropy (Bassez 2016) involving water in its high subcritical domain, for the formation of ferric minerals inside the Earth crust, followed by the synthesis of molecules of life inside mineral cavities (Bassez 2013–2022).

The present article experimentally confirms the theoretical propositions. Spectroscopic investigations have been conducted on an Archean sample of ferruginous chert. The chosen sample is a section from the BARB3 core that was drilled inside the 3.416 Ga Buck Reef chert, South Africa. Preference was given to a Paleoarchean age instead of a Neoarchean age, for certainty that dissolved oxygen was absent from the oceans at the time of its formation. An earlier study of the same area is reported in (Hofmann et al. 2013a). The Hofmann outcropping samples are from sedimentary black cherts, while the BARB3_23B drilled sample is from a banded ferruginous chert in the form of a short banded iron sequence. A comparison of the results from the black cherts and the BARB3_23B sample is described in the last paragraph of the section on "disordered graphitic carbon", in the first section of "Results".

The article reports spectroscopic analyses and interpretations of data recorded with three different Raman instruments between 2019 and 2021 and supplements an earlier report of quartz and siderite that were recorded with a fourth Raman instrument (Bassez 2018). The results described here show the presence of hematite, of alternate layers of quartz-hematite and quartz-siderite, and of possibly greenalite in the quartz matrix. Gaseous methane, strongly basic water and possibly Fe^{III}-greenalite are present inside the quartz cavities. The importance of considering water in its high subcritical domain is emphasized for the formation of Archean methane and disordered graphitic carbon. It is proposed that methane can form at the location of ferrous silicate rocks inside the Earth crust, following the interaction of the CO_2 dissolved in high subcritical water with the H_2 emitted during the anoxic alkaline oxidation of Fe^{2+} by high subcritical water. The observed disordered graphitic carbon is proposed to have been deposited from this Archean methane-rich fluid. The entire chemical composition of the BARB3_23B banded layers is predicted by the theoretical model.

Raman spectra of the carbon matter from the BARB3_23B drilled sample resemble those reported in (Hofmann et al. 2013a) for the outcropping sample. Wondering if the origin of the disordered graphitic carbon matter might be in the process of fabrication of the thin sections, a detailed study of Raman spectra of carbon matter from diverse origins has been undertaken and is described in the supplementary file: *"The BARB3_23B disordered graphitic carbon"*. The conclusion is that a possible direct relation can exist between Raman profiles of disordered graphitic carbon and the amounts of functional groups containing oxygen, and that the BARB3_23B disordered graphitic structure contains very few oxygen, no hydroxyl functional groups and has been submitted to ~ 335 °C, a temperature of the high subcritical domain.

Following the importance of considering water in its high subcritical domain of temperature, pressure and density, hypotheses for the formation in the Earth crust of the minerals observed in the Archean banded iron formations, BIFs, and the Neoproterozoic banded iron formations, NIFs, are proposed.

The article successively presents the results obtained with four different Raman spectrometers on single point spectra, lines of spectra, maps and with acute observations of quartz cavities. Then is proposed a possible formation of an Archean methane-rich fluid at the location of ferrous silicate oxidation, and of a graphitic carbon deposition. Finally, a hypothesis for the formation of BIFs and NIFs, with a relation to subduction events or not, is presented with two figures that are improved from (Bassez 2019a, b, 2022) and one figure which describes the three levels of intervention of water in its high subcritical domain. Experiments on the oxidation of Fe^{2+} near the supercritical point of water are proposed. Their results will confirm the importance of considering water in its high subcritical domain and above, in geological environments. They will also provide the knowledge on the redox behavior of the system Fe—supercritical water which is at present unknown. The majority of the sections contains one non-indented sentence or small paragraph which introduces the section, one non-indented conclusion, and details of the demonstration between both.

The Sample: Geological Setting and Methods of Observations with Highlighted Results

The present results concern one section of the 3.4 Ga Buck Reef Chert, located in the Onverwacht group of the Barberton greenstone belt in the Kaapvaal craton, South Africa. Four different Raman microscopes were used for the observations.

The Buck Reef Chert, BRC, is dated to 3.416 Ga in age, following analyses of *"zircons from a dacitic tuffaceous sandstone"* (Kröner et al. 1991 §3.1) in the uppermost part of the felsic volcanic unit of the Hooggenoeg Formation at the west end of the Onverwacht Anticline. The BRC crops out over more than 30 km (Tice and Lowe 2006; Ledevin et al. 2019), covering the 3.445 Ga member H6 unit of Hooggenoeg. *"It overlies a shallow intrusive to extrusive sequence of dacitic volcanic rocks of the Hooggenoeg formation and is separated from ultramafic lapillistone of the bottom of the Kromberg formation by a > 150 m thick ultramafic sill"* (Hofmann et al. 2013b). The location of the BRC is drawn on a geological map showing the Onverwacht Anticline and on a stratigraphic column in (Hofmann et al. 2013a; Figs. 1 and 2, position number 4). Four sections compose the Buck Reef: silicified evaporite at the base, black and white banded chert, banded ferruginous chert and an upper section of black and white chert(Lowe and Byerly 1999 p.13). The 3.4 Ga Buck Reef Chert, named by Hall in 1918

(Lowe and Byerly 1999 p.13) was renamed the Buck Ridge Chert of the 3.45–3.42 Ga volcanic-sedimentary complex, BRVC, (de Vries et al. 2006) and then the Noisy Complex or Noisy Formation (de Wit et al. 2011). *"The BRVC is capped by the ~ 400 m thick Buck Reef Chert"* (Agangi et al. 2018). To investigate early Earth processes, the BARB3 drill was conducted inside the Buck Reef Chert in 2011. *"Drilling commenced in the ultramafic sill at an angle of c. 45° and c. 200 m of serpentinized peridotite were intersected... The BRC is an unusually thick (up to 350 m) sequence of predominantly black-and-white banded chert and banded ferruginous chert that are steeply dipping."* (Hofmann et al. 2013b). Upon the technical sheet of the drill (personal communications from Arndt and Hofmann 2021), the coordinates in decimal degrees are 25.928467° S, 30.925593° E at the start of the drill and 25.932131° S, 30.923019° E at the end of the drill. Elevations are 1635 m and 1073 m at the start and end, respectively. Figure 1 shows three Google map images of the Barberton Greenstone belt and the Buck Reef chert with the coordinates of the drill. Figure 1d shows a photograph of the BRC hill taken by the ICDP, International Continental scientific Drilling Program, for the Barberton Drilling Project: Peering into the Cradle of Life: *"General view of Buck Reef. The drill hole will be sited at the level of the trees on the horizon and will penetrate 800 m through the bedded cherts."* (ICDP 2011). Figure 1d includes a diagram of the drill intersecting the BRC layers. The BRC hill is slightly tilted. Because of the tilt, the
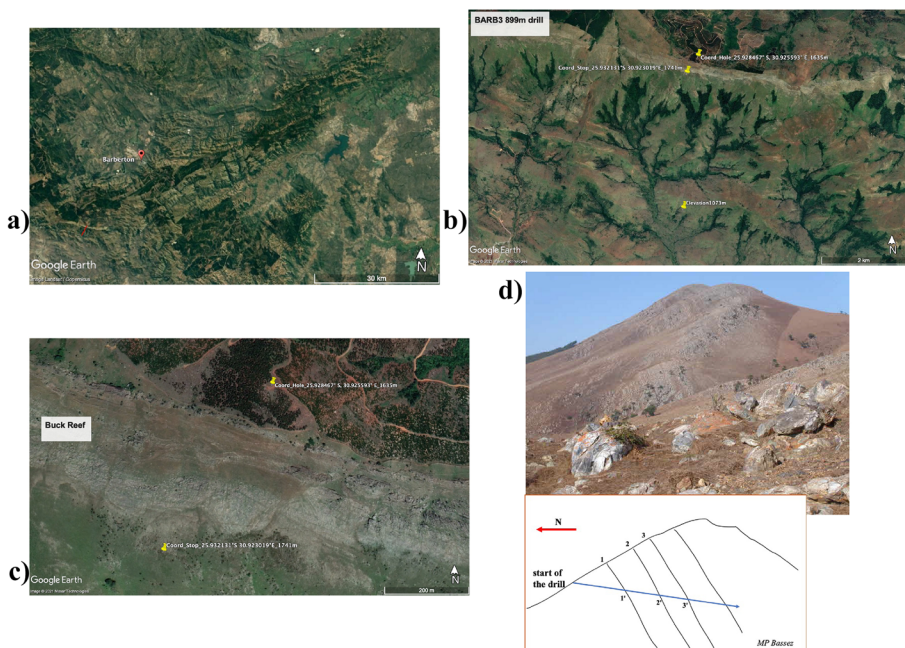

Fig. 1 The Buck Reef Chert, Barberton Greenstone Belt, Kaapvaal Craton, South Africa. **a)** The Barberton Greenstone Belt. The red line on the bottom left indicates the location of the drill inside the Buck Reef Chert **b)** Coordinates of the start of the drill, "Coord_Hole", at elevation 1635 m, and of the end of the drill, "Coord_Stop", at elevation 1073 m. The 899 m long drill was conducted at an angle of 39° and ended at an elevation of 1073 m, vertical to "Coord_Stop" **c)** The Buck Reef **d)** ICDP photograph of the Buck Reef hill. The drill starts at the level of the trees; Diagram showing the tilted hill and the drill that crosses the layers of chert. 3 is younger than 2, which is younger than 1. The drill advances towards younger samples

drill advances towards younger layers. The drill core has a total length of 899 m (Arndt et al. 2012). The sample studied in the present article is located between 471.26 m and 471.48 m towards the middle of the drill core.

The studied sample is the polished thin section BARB3_23B, 2 cm×4 cm×30 μm, which was constructed from a quarter-round fragment adjacent to the one of Fig. 2. To date, it is the unique representative of the colorful banded layers located in the middle of the BARB3 core.

A first set of observations of the thin section was conducted with Raman spectroscopy on a suite of single points, at the University of Johannesburg, South Africa, in March 2018. The instrument was a WITec Alpha300 R confocal Raman spectrometer composed of a confocal microscope coupled to a Raman spectroscope. The excitation radiation was emitted from a Nd:YAG laser operating at the green wavelength of 532 nm (2.34 eV), and the wavelength calibration of the spectrometer was achieved daily with the peak of a pure crystalline silicon wafer. The grating was operating at 600 and 1800 grooves/mm. The Project FIVE 5.1 WITec software for curve fitting was used to determine the Raman shift wavenumbers. The 2018 spectroscopic analyses of single spectra indicate the presence of the minerals quartz and siderite. They are published in (Bassez 2018).

Observations of the thin section were further conducted on an identical instrument, the WITec Alpha300 R confocal Raman spectrometer, on the CY Microscopy and Analysis platform of La Maison de la Recherche, Cergy Paris Université, Neuville-sur-Oise, France, on December 10th, 2019 and January 30th, 2020. The excitation laser was tuned to 532 nm. The laser power was set to 10 mW and not measured at the sample with an external power meter. The acquisition time was 2×1 s per laser irradiation, and the detection grating was engraved with 600 grooves/mm. The magnification of the objective was 50x. Its numerical aperture, NA, 0.80, produced a laser spot size of ~1 μm when the beam was well focused. The Project FIVE 5.1 WITec software for curve fitting was used to determine the Raman shift wavenumbers. The results of the 2020 set of observations are shown in Figs. 3 to 8. They confirm the earlier observations of quartz and siderite (Bassez 2018) and conclude in the presence of hematite and disordered graphitic carbon, and of alternate layers of quartz-hematite and quartz-siderite.
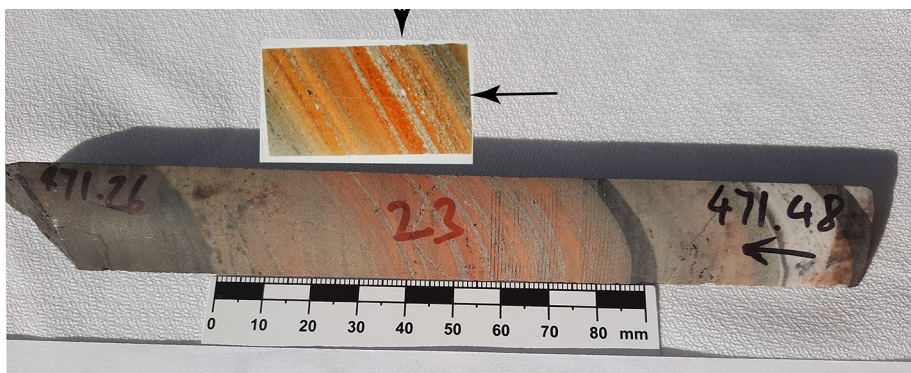

Fig. 2 The BARB3_23B sample. A quarter-round core fragment from the drill hole BARB3, located between drill depths of 471.26 m and 471.48 m, and the studied polished thin section, 2 cm×4 cm×30 μm, which was cut in the adjacent quarter-round core. The arrows indicate the white ~1.20 mm quartz grain studied with Raman maps in Figs. 9 to 11, and for fluid inclusions in Figs. 13 to 15
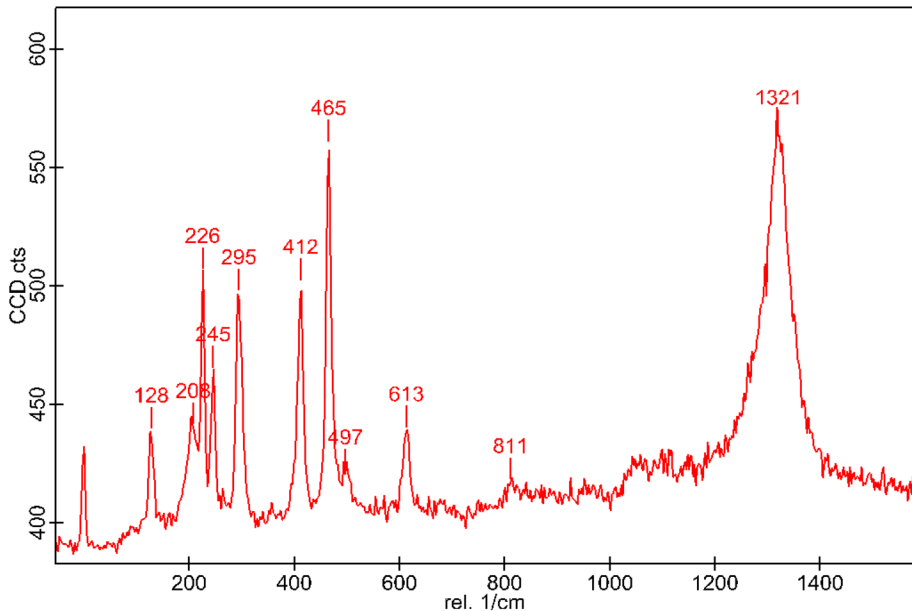
Fig. 3 Raman spectrum of quartz and hematite, recorded on a single point of the orange layers of the Buck Reef chert BARB3_23B thin section. It is characteristic of the Raman spectra that are recorded on single points of the orange layers, and on the lines of Figs. 5 and 6. The well-resolved peaks at 226 cm^{-1}, 245 cm^{-1}, 295 cm^{-1}, 412 cm^{-1}, 613 cm^{-1} and 1321 cm^{-1} are assigned to hematite, as well as the poorly resolved peaks at ca. 497 cm^{-1}, 811 cm^{-1}, 1050 cm^{-1} and 1100 cm^{-1}. The peaks appearing at 128 cm^{-1}, 208 cm^{-1} and 465 cm^{-1} are characteristic of quartz

A third set of observations was conducted with optical images and Raman maps that were recorded and data processed at the CBM, Centre de Biophysique Moléculaire, CNRS, Orléans, France, on July 27th and 28th 2021, with a WITec Alpha500 RA confocal Raman spectrometer and its software. The frequency doubled Nd:YAG laser was operating at 532 nm, and the grating at 600 grooves/mm produced an average spectral resolution of ca. 4 cm^{-1}. Raman imaging consists of scanning the sample continuously, line by line, while acquiring spectra. The spatial resolution corresponds to the ratio of the length of the line over the number of spectra acquired per line. The distance between each line is chosen to obtain square pixels. Each spectrum of a scan corresponds to the average spectrum collected over a line of thickness equal to the spot size diameter and of length equal to the pixel size. Raman images of concentrations are obtained by associating a color scale to the area of a given peak representative of a specific phase, for instance, the peak at 465 cm^{-1} for the quartz. The G band is used to display carbonaceous matter because of the strong hematite band at ~1320 cm^{-1} that may overlap the D band. More information about Raman imaging can be found in Foucher et al. (2017). The results are shown in Figs. 9 to 11. Figure 12 recorded at CY Cergy Paris, shows the resine glue for comparison. The Raman maps show the distribution of the minerals and conclude that the disordered graphitic carbon seems distributed on the entire scanned area. The 2021 analyses of Raman shifts confirm the published 2018 observations of quartz and siderite, and the unpublished 2019–2020 observations of hematite and disordered graphitic carbon. In addition, they indicate the plausible presence of the silicate greenalite.

A fourth set of observations conducted with optical images and Raman single spectra was recorded and data processed at the Laboratoire de Génie Civil et géo-Environnement, LGCgE, University of Lille, France, on March 10, 2020 and from August 12 to August 19, 2021. The microscope used to recognize the fluid inclusions was an Olympus BX 60. With the objective of 100x and the ocular 25x, fluid inclusions of 3.25 μm in size could be recognized as shown on Figs. 13 and 14. The Raman instrument was a Horiba Jobin Yvon HR 800 Raman spectrometer. The excitation radiation was provided by an Ar Lexel laser tuned at 532 nm. The Raman vibrational process was used to identify liquid water, methane and either greenalite or sodium hydroxide in very small fluid inclusions. The results are shown on Fig. 15.

The assignment of the BARB3_23B Raman peaks was done by comparison with the Raman shifts reported in the RRUFF data base and in articles written by other authors.

Results. Quartz, Siderite, Hematite and Graphitic Carbon Observed on Single Points and Along Lines. Alternate Layers of Hematite and Siderite

All spectra and images were recorded at CY Cergy Paris. They are presented without smoothing or background correction. The appellations of the peaks and parameters of the graphitic carbon are described in the supplementary file.

Quartz, Siderite, Hematite

The silicate quartz, the carbonate siderite and the oxide hematite are identified.

Figure 3 shows the Raman spectrum of hematite which is identified with observations conducted on single points (Fig. 3) and lines of points (Figs. 5 and 6). The profile is characteristic of all the spectra marked "Q, Hem" that are recorded along the lines (Figs. 5, 6). By comparison with the RRUFF spectra, the well-resolved peaks at 226 cm^{-1}, 245 cm^{-1}, 295 cm^{-1}, 412 cm^{-1}, 613 cm^{-1} and 1321 cm^{-1} are assigned to hematite, as well as the poorly resolved peaks at~49 7 cm^{-1}, ~811 cm^{-1}, ~1050 cm^{-1} and~1100 cm^{-1}. The peaks appearing at 128 cm^{-1}, 208 cm^{-1} and 465 cm^{-1} are characteristic of quartz as reported in (Bassez 2018, Table 3).

Figure 4 shows a stitching optical image, 5 mm wide by 2 cm high. The two blue and red vertical lines show the positions of the continuous laser irradiations. The lines of spectra were recorded separately from the optical image and consecutively applied with the Witec software on the optical image. The spectra are displayed on Figs. 5 and 6.

Figures 5 and 6 show the upper and lower parts of Fig. 4 together with spectra that are recorded along the lines. Spectra of pure quartz, Q, alternate with spectra of pure siderite, Sid, inside the greyish layers, and spectra of pure quartz, Q, alternate with spectra of quartz and hematite, Q, Hem, inside the reddish layers. The borders between the quartz-siderite and quartz-hematite are not sharp. Some siderite is observed inside the reddish layers and hematite peaks occur inside the greyish layers.

Figure 7 shows the spectrum of quartz and siderite recorded at the yellow cross, which is also yellow in Fig. 4. The peaks at 128 cm^{-1}, 206 cm^{-1}, 356 cm^{-1}, 401 cm^{-1} and 465 cm^{-1} are assigned to quartz. The peaks appearing at 295 cm^{-1} and 1089 cm^{-1} are assigned to siderite. The 192 cm^{-1} peak usually assigned to siderite seems connected to the 206 cm^{-1} quartz peak.

Fig. 4 Mosaic of optical images showing 5×20 mm^2 of the central part of the Buck Reef chert BARB3_23B. Two lines of Raman observations are shown in blue and red. The minerals observed along the lines are displayed on Figs. 5 and 6. The green cross is at the same location than the green cross on Fig. 6 and the red cross on Fig. 8 and corresponds to the spectrum of siderite and carbon shown on Fig. 6. The yellow cross corresponds to the lowest position that produces the spectrum of quartz and carbon on Fig. 5
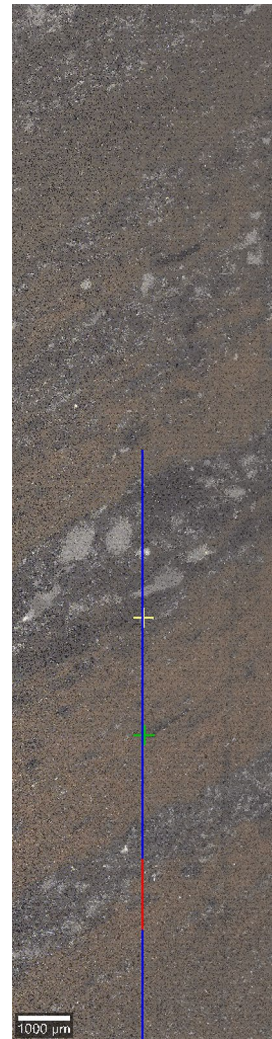
Figure 8 shows the spectrum of siderite and disordered graphitic carbon recorded at the position of the red cross, which is the position of the green crosses on Figs. 4 and 6. The peaks at 192 cm^{-1}, 296 cm^{-1} and 1089 cm^{-1} can be unambiguously assigned to siderite. Siderite reported in (Bassez 2018) is thus confirmed with the observations on lines of points (Figs. 5 and 6) and on single points (Figs. 7 and 8). The peaks at 1344 cm^{-1} and 1599 cm^{-1} together with the three imperfectly resolved peaks at ~ 2677, ~ 2923 and ~ 3200 cm^{-1} are assigned to disordered graphitic carbon. They appear with the same Raman profile for all black grains of Figs. 7 and 8, which are all optically observed with ~ 4 to ~ 20 μm sizes.
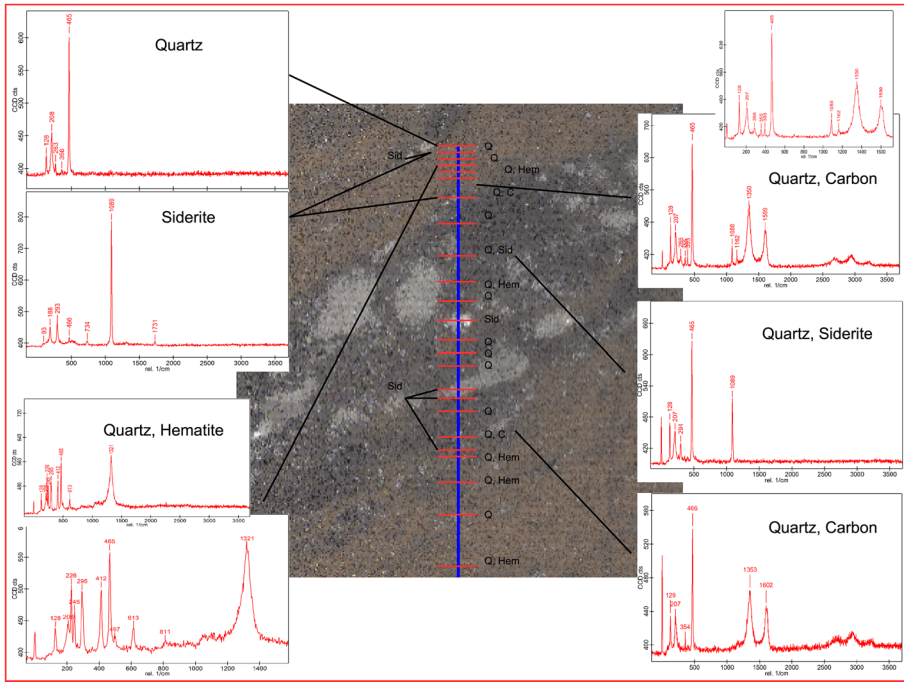
Fig. 5 Upper part of the mosaic optical image of the Buck Reef chert BARB3_23B shown on Fig. 4, and the corresponding Raman spectra continuously recorded along the lines. The red horizontal lines show the positions of selected laser irradiations. They are marked: "Q" for a spectrum displaying only quartz, "Sid" only siderite, "Q, Hem" quartz and hematite, "Q, C" quartz and carbon, "Q, Sid" quartz and siderite. All locations marked "Q, Hem" show identical spectra to the one reported on Fig. 3. The lowest "Q, C" spectrum is recorded at the position of the yellow cross of Fig. 4. The upper reddish band of the thin section displays a succession of quartz and quartz with hematite. The greyish band is composed of a large dark grey area made of quartz and clearer grey grains made of siderite

Disordered Graphitic Carbon

The peaks of graphitic carbon appear either with the siderite peaks (Fig. 8, and green crosses of Figs. 4 and 6) or with the quartz peaks (lower part of Fig. 6).

Their Raman shifts are averaged to 1348 ± 5 cm^{-1} and 1601 ± 5 cm^{-1}. For instance, the siderite and carbon spectrum on Fig. 6, which is extracted from the line of Raman spectra, shows peaks at 1353 cm^{-1} and 1604 cm^{-1}. The corresponding single point spectrum that is recorded at the position of the green cross on the line of Fig. 6, and that is drawn as a red cross on Fig. 8a, is shown in Fig. 8b with peaks at 1344 cm^{-1} and 1599 cm^{-1}. The quartz and carbon spectrum of Fig. 6, extracted from the line, shows peaks at 1345 cm^{-1} and 1606 cm^{-1}. The two quartz and carbon spectra of Fig. 5 that are extracted from the line, show peaks at 1350 cm^{-1}, 1599 cm^{-1}, and 1353 cm^{-1}, 1602 cm^{-1}. All these values are within 5 cm^{-1} of the retained values 1348 cm^{-1} and 1601 cm^{-1}. All the ~ 1348 cm^{-1} peaks appear symmetrical with no foot at low wavenumbers. They can be assigned to the D band with the D_4 band at ~ 1200 cm^{-1} which is absent. All the ~ 1601 cm^{-1} peaks appear symmetrical with no shoulder at higher wavenumbers. They can be assigned to the 1582 cm^{-1} G band associated with the 1620 cm^{-1} D_2 (or D') band. In all spectra, the level between the D and G peaks is higher
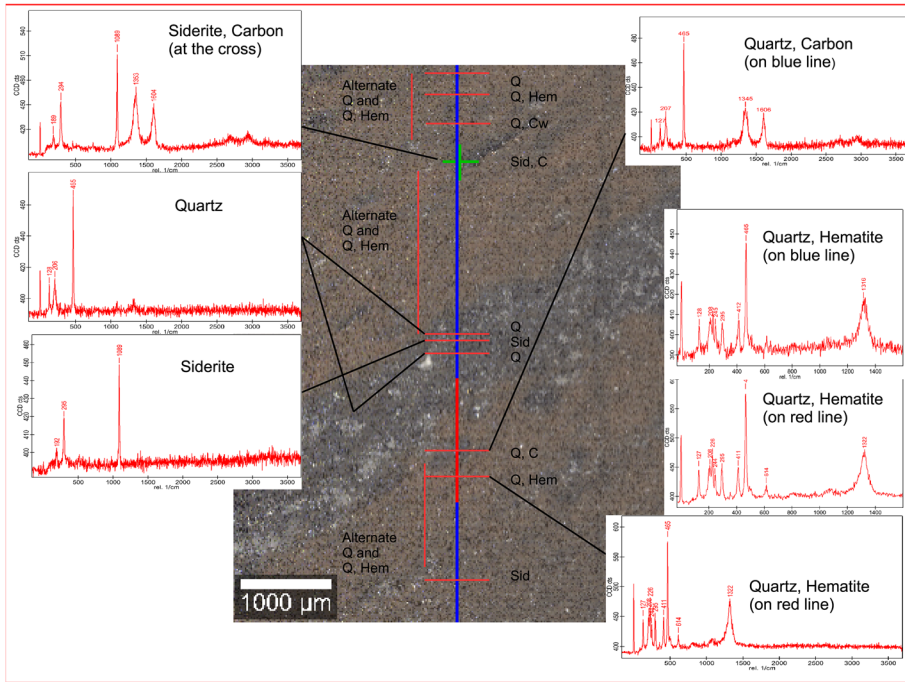
Fig. 6 Lower part of the mosaic optical image of the Buck Reef chert BARB3_23B shown on Fig. 4, and the corresponding Raman spectra continuously recorded along the lines. The red horizontal lines show the positions of selected laser irradiations. They are marked: "Q" for a spectrum displaying only quartz, "Sid" only siderite, "Q, Hem" quartz and hematite, "Q, C" quartz and carbon (w is for weak intensity), "Q, Sid" quartz and siderite, "Sid, C" siderite and carbon. All locations marked "Q, Hem" show identical spectra to the one reported on Fig. 3. At the position of the green cross, the spectrum extracted from the line shows siderite and carbon. The corresponding spectrum taken on a single point at the green cross is shown on Fig. 8b. The upper reddish band of the thin section displays a succession of quartz and quartz with hematite. The greyish band is composed of a large dark grey area made of quartz and clearer grey grains made of siderite

than the background level. This shape may indicate either an underlying band as described in (Sadezky et al. 2005; Marshall et al. 2010; Delarue et al. 2016) considering a curve fitting procedure on three or four peaks, or no underlying band, as in (Bonal et al. 2016 Fig. 1a) where curve fitting is applied with only two peaks, a Lorentzian curve on the D peak and a Breit–Wigner–Fano curve on the G peak. Considering the two methods of fitting, the D_3 band at ~1500 cm^{-1} may or may not be in the Buck Reef BARB3_23B sample.

The three broad peaks at ~2677, 2923 and 3200 cm^{-1} can be assigned to the 2D, $(D+D_2)$ and $2D_2$ bands respectively. The peak parameters that I calculate graphically by hand are ~1.3 ± 0.1 for I_D/I_G, ~70 ± 4 cm^{-1} for the D band FWHM, ~50 ± 2 cm^{-1} for the G band FWHM, and ~0.67 for the D/(D+G+D') ratio, also named the R2 area ratio. All these values lead to the identification of the carbon matter as disordered graphitic carbon.

Hofmann et al. (2013a) *"investigated…bedded cherts and associated chert veins from several stratigraphic levels of the BGB, ranging in age from ~3.48 to ~3.26 Ga".* Their studies were conducted on the western part of the Barberton greenstone belt in the Onverwacht Group from the top of the Komati Formation (Middle Marker) through the Hooggenoeg Formation, including the Buck Reef Chert and the Kromberg
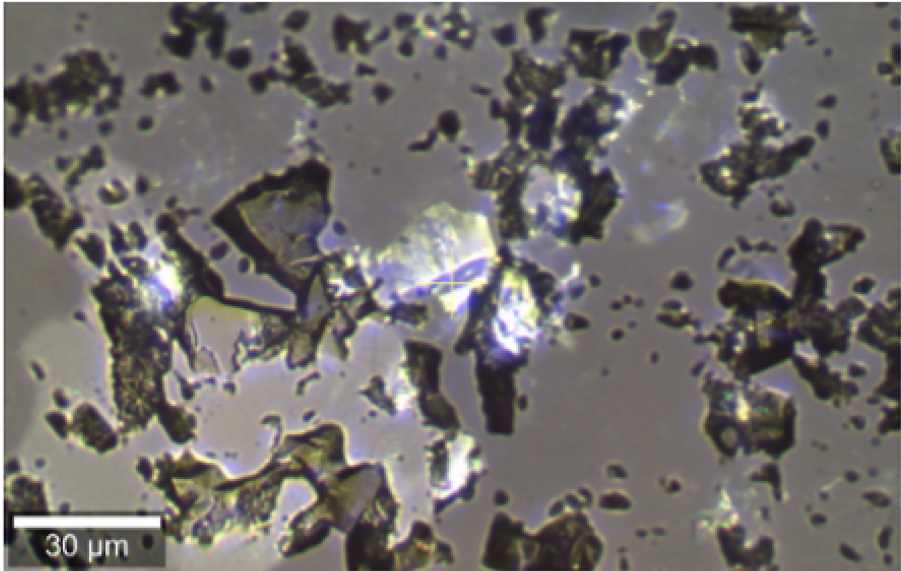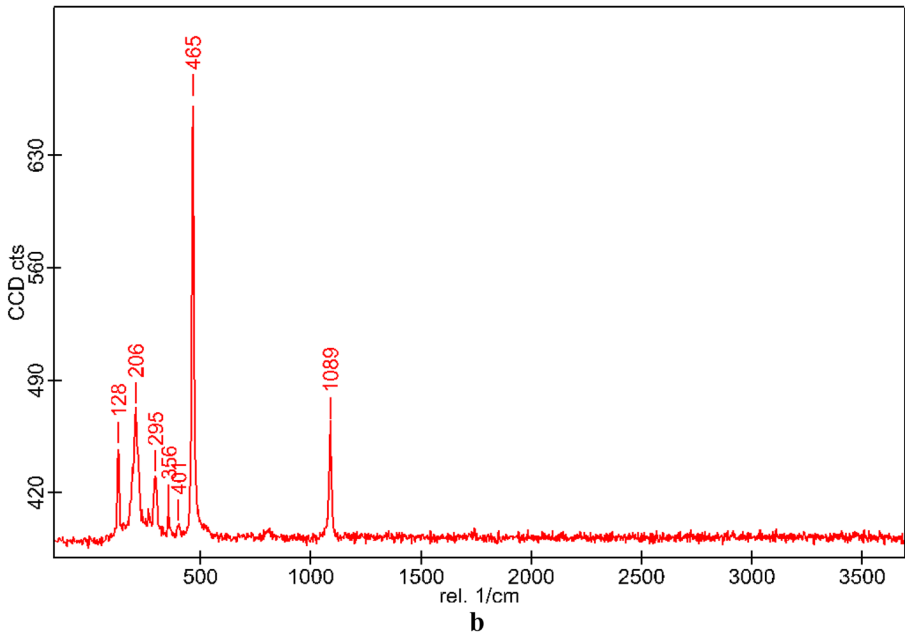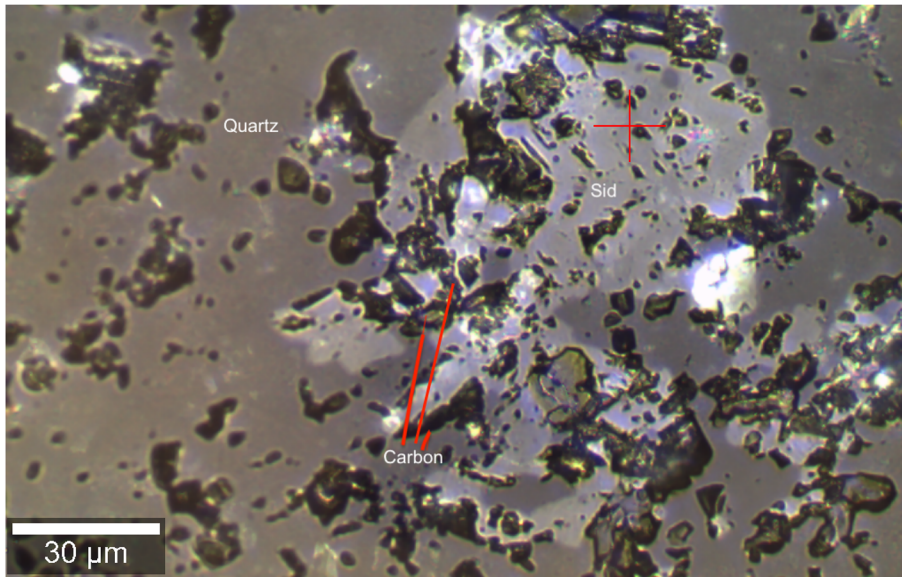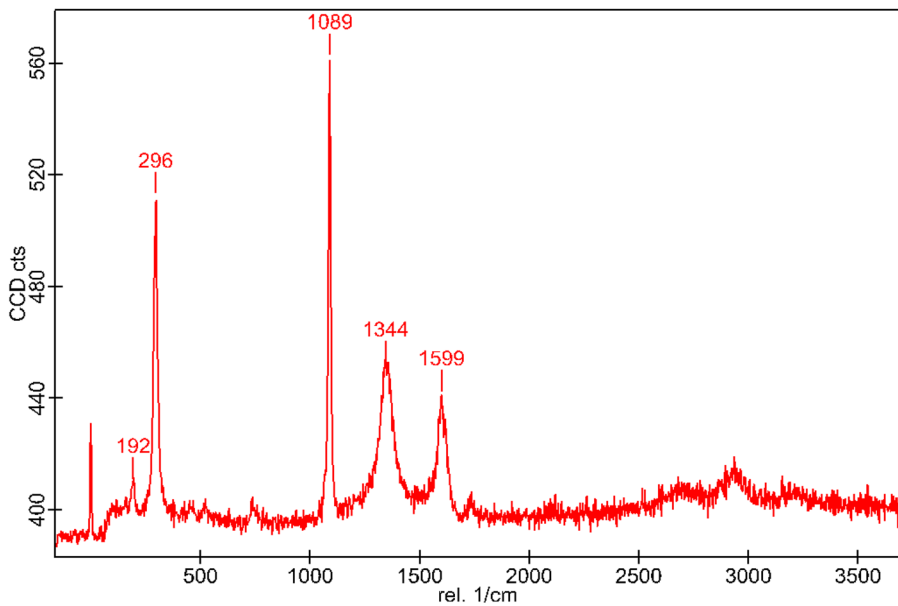
a

b

Fig. 7 Quartz and siderite observed on a single point of the Buck Reef chert BARB3_23B **a)** Single optical image showing the point of laser irradiation (yellow cross) and its environment **b)** Raman spectrum recorded on a single point at the yellow cross position, which is applied as a yellow cross on Fig. 4. The characteristic peaks are those of siderite at 295 cm^{-1}, 1089 cm^{-1}, and quartz at 128 cm^{-1}, 206 cm^{-1}, 356 cm^{-1}, 401 cm^{-1} and 465 cm^{-1}. The 192 cm^{-1} siderite peak observed on Fig. 7b seems to broaden the 206 cm^{-1} peak of quartz

a

b

Fig. 8 Siderite and disordered graphitic carbon observed on a single point of the Buck Reef chert BARB3_23B **a)** Single optical image showing the point of laser irradiation (red cross) and its environment. All black aggregates are composed of disordered graphitic carbon **b)** Raman spectrum recorded on a single point at the red cross position, which is applied as a green cross on Figs. 4 and 6. The characteristic peaks are those of siderite at 192 cm^{-1}, 296 cm^{-1}, 1089 cm^{-1}, and disordered graphitic carbon (D, G+D', 2D, D+D', 2D' respectively) at 1344 cm^{-1}, 1599 cm^{-1}, $\sim$2700 cm^{-1}, $\sim$2923 cm^{-1} and $\sim$3200 cm^{-1}. The Raman spectrum which is extracted from the line of spectra at the position of the green cross on Fig. 6, shows also siderite and disordered graphitic carbon

Formation, up to the top of the Mendon Formation. As described, *"the Buck Reef Chert…consists of a sequence of black-and-white banded chert and banded ferruginous chert…Three samples of sedimentary black chert have been analyzed… together with one sample from a black chert vein".* Samples from outcrops were studied with the 532 nm Raman spectrometer, of the Witec Alpha500 RA instrument, at CBM, CNRS, Orléans, France. Their Fig. 12 shows spectra observed at single points for four samples of bedded cherts in the Hooggenoeg, BRC, Kromberg and Mendon Formations. All four spectra show equivalent first-order peaks, with parameters that I calculate by hand to be ~1600 cm^{-1} for the G peak, ~1342 cm^{-1} for the D peak, and ~63 cm^{-1} for both D and G FWHMs. The D_4 band at ~1200 cm^{-1} is absent. Their Fig. 9 compares the carbon matter in the bedded and vein cherts of the Hooggenoeg Formation. Both first- and second-order spectra appear equivalent, with the peak that I calculate to be at ~2689 cm^{-1}, slightly more intense than the ~2944 cm^{-1} peak. The BARB3_23B peak at ~3200 cm^{-1} is absent. Their Fig. 10 displays Raman spectra of the carbon matter in the bedded and vein cherts of the BRC. Both first-order spectra appear identical, except for an increase in the G band intensity for the vein chert. These spectra of carbon matter from bedded and vein cherts from four outcropping stratigraphic levels show identical profiles to those of the BIF from the drilled BARB3_23B sample studied here, with the same shifts for the G, D and second-order peaks, approximately the same FWHMs, and the absence of the D_4 peak. The differences are in the I_D/I_G intensity ratios and FWHMs. The I_D/I_G that I calculate by hand as 2.2 for the outcrop, a value equivalent to what is reported in the Hofmann text, is much higher than for the BARB3_23B ratio that I calculate likewise by hand as 1.3 ± 0.1. Both D and G widths of the outcrop are ~63 cm^{-1}, while the BARB3_23B D width is slightly wider than the G width (70 ± 4 and 50 ± 2 cm^{-1} respectively). The reported grain sizes are much larger for the outcrop than for BARB3_23B. Both bedded and vein cherts of the BRC outcropping samples contain as reported *"irregular grains…up to 1 mm in diameter…200 µm across"* with a higher concentration in the bedded chert (Hofmann Fig. 3A, B) while BARB3_23B contains grain sizes of 4 to 20 µm (Figs. 7a and 8a). The mineral content of the outcropping BGB samples was studied with Raman spectroscopy and EDS-SEM observations, while BARB3_23B was studied only with Raman spectroscopy. The mineralogy of the outcropping black chert appears much more complex than the mineralogy of the BARB3_23B from a drilled banded ferruginous chert. Table 2 in (Hofmann et al. 2013a) shows that the black chert is composed of the silicates chlorite, K-mica, K-feldspar, the carbonates dolomite and Mn-Mg bearing calcite, the sulfates alunite/jarosite, the phosphates apatite, monazite, the Co–Ni-As-Fe sulfides and chalcopyrite, and oxides of Ti, Fe and Cr. Despite this huge variation in mineralogy, the carbon matter seems almost the same, with the drilled BIF appearing more graphitized (lower I_D/I_G).

Results. Distribution of Quartz, Hematite, Siderite and Graphitic Carbon on Raman Maps

Raman spectral imaging shows the interconnection between the minerals quartz, hematite and siderite, the alternate layers of siderite and hematite on a quartz matrix, and the distribution of disordered graphitic carbon.

Raman maps acquired on the Buck Reef Chert BARB3_23B thin section are displayed on Figs. 9 to 11. They were recorded and data processed at the CBM, CNRS, Orléans. Figure 9a displays a stitching or mosaic optical image of the quartz grain, shown with arrows on Fig. 2, and of its surroundings. Figures 9b-e display four spectral images or Raman maps of the individual minerals, quartz, siderite, hematite and of carbon matter. Figure 9f displays one spectral image of the combined minerals and carbon matter. Figure 9g shows the average spectra of the observed phases. The chosen grating was 600 grooves/mm, producing a spectral resolution of 5 cm^{-1} at low wavenumbers and 3 cm^{-1} at high wavenumbers. The laser wavelength was 532 nm. The laser power was measured with a power meter, to be 5 mW at the output of the objective. The characteristic peaks appear at 128 cm^{-1}, 205 cm^{-1}, 464 cm^{-1} for quartz, 190 cm^{-1}, 296 cm^{-1}, 1089 cm^{-1} for siderite and 293 cm^{-1}, 412 cm^{-1}, 1320 cm^{-1} for hematite. Within the spectral resolution of ~4 cm^{-1}, the Raman shift wavenumbers appear at the same position as those of the spectra recorded on single points (Figs. 3 to 8). The peaks at 1329 cm^{-1} and 1599 cm^{-1} appear very noisy. The value 1329 seems distant from the value obtained with laser irradiations of single points and lines, as described above and in the section on the BARB3_23B carbon matter, which reports 1348±5 cm^{-1} and 1601±5 cm^{-1} for the D and G bands, respectively. The apparent low value of the D band (1329) is explained by the overlapping of the hematite signal. Quartz is uniformly distributed while hematite and siderite alternate (Fig. 9c, d). The carbon matter seems homogenously distributed with perhaps a higher concentration which can be discerned on the siderite parts. The results confirm and illustrate the
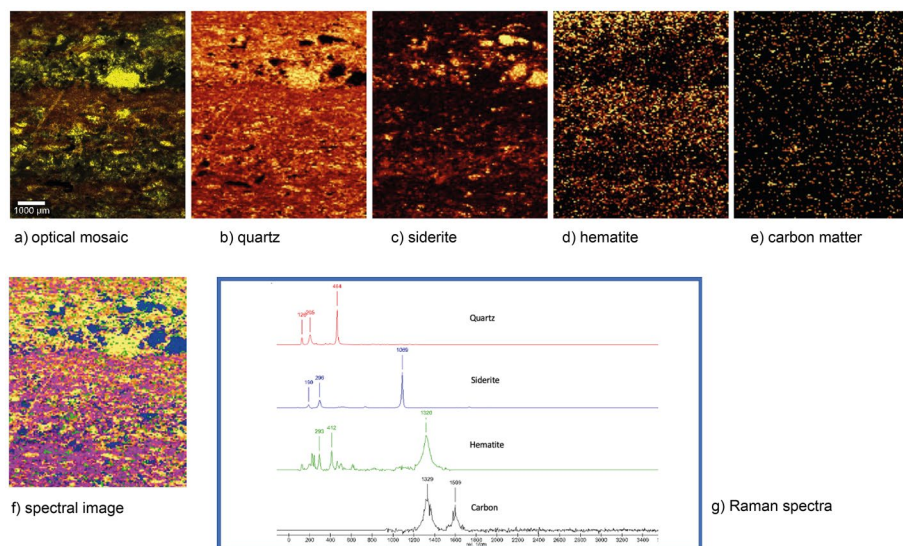

a) optical mosaic   b) quartz   c) siderite   d) hematite   e) carbon matter

f) spectral image   g) Raman spectra

Fig. 9 The quartz grain of the Buck Reef chert BARB3_23B observed on Fig. 2 (in the direction of the arrows) and its nearest surroundings **a)** Mosaic of optical images **b)**, **c)**, **d)**, **e)** Four spectral Raman images or Raman maps of individual minerals and of carbon matter. The highest concentration is colored in bright yellow **f)** Spectral Raman map of the combined minerals and carbon matter: quartz in yellow, siderite in blue, hematite in fuchsia, carbon matter CM in green **g)** Average Raman spectra of all the spectra recorded during the scan for each component. 532 nm laser, 5 mW laser power at the objective, acquisition time 0.3 s/spectrum, 130 spectra/line, 154 lines, total number of spectra 20,020, WITec Alpha500RA, CBM, CNRS, Orléans
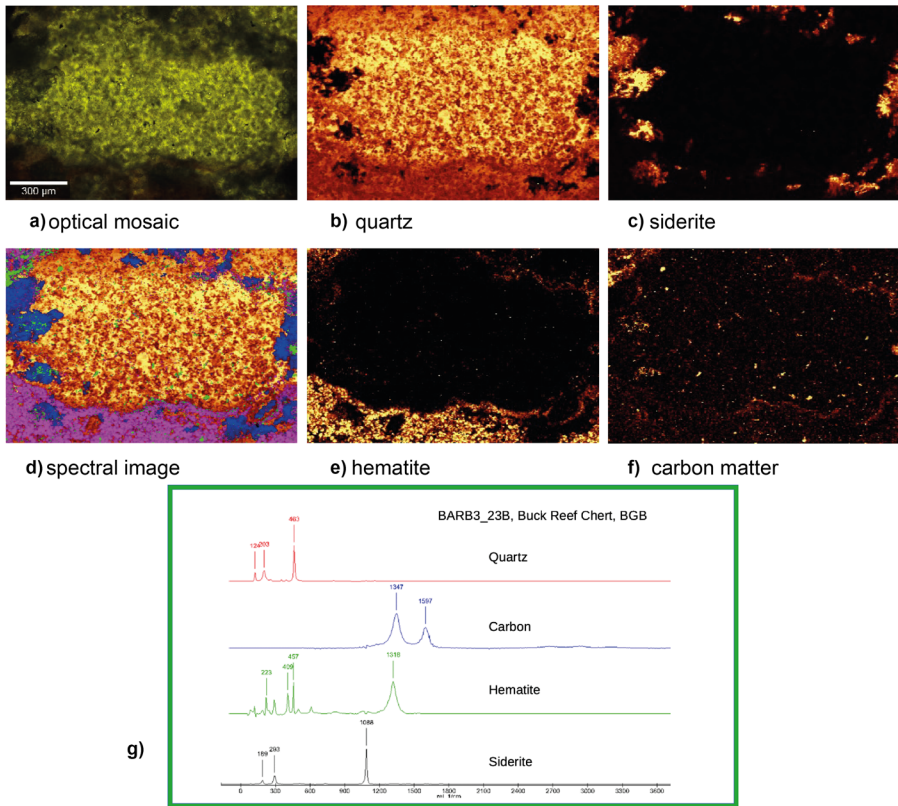
Fig. 10 The quartz grain of the Buck Reef chert BARB3_23B shown on Figs. 2 and 9 **a)** Mosaic of optical images **b)**, **c)**, **e)**, **f)** Spectral Raman images or Raman maps of individual minerals and of carbon matter **d)** Spectral Raman map of the combined minerals and carbon matter: quartz in yellow, siderite in blue, hematite in fuchsia, carbon matter CM in green; the carbon matter spectral image is constructed with the G band **g)** Average Raman spectra of all the spectra recorded during the scan for each component. 532 nm laser, 14 mW laser power at the objective, acquisition time 0.6 s/spectrum, 375 spectra/line, 250 lines, total number of spectra 93,750, WITec Alpha500RA, CBM, CNRS, Orléans

observations and analyses conducted at Johannesburg (Bassez 2018) and the unpublished observations and analyses conducted at CY Cergy Paris on single point and lines of spectra (Figs. 3 to 8) and clearly show the alternate layers.

Figure 10 displays a larger magnification of the quartz grain of Fig. 9, with Raman maps and spectra. The carbon matter seems to be distributed above quartz and hematite with perhaps a greater concentration in the areae of siderite. The laser power was 14 mW at the objective. The characteristic peaks appear at 124 cm^{-1}, 203 cm^{-1}, 463 cm^{-1} for quartz, 189 cm^{-1}, 293 cm^{-1}, 1088 cm^{-1} for siderite and 223 cm^{-1}, 409 cm^{-1}, 1318 cm^{-1} for hematite. The Raman shifts of the graphitic carbon D and G bands which appear at 1347 cm^{-1} and 1597 cm^{-1} are equivalent to those recorded with single point laser irradiations at CY Cergy Paris with a laser power set to 10 mW (Figs. 5, 6 and 8).

Results. Greenalite Inside the Quartz Matrix

The Raman peaks at 632 and 1028 cm^{-1} are assigned to the mineral greenalite.

Figure 11 displays four different magnifications of the quartz crystal of Figs. 9 and 10. The Raman spectrum was taken at the position of the red cross and was recorded with a 100x (NA 0.9) objective, a laser power of 14 mW and 300 s integration time, at the CBM, Orléans.

The characteristic peaks of quartz at 126, 205, 464 cm^{-1} are present. The peaks at 406 and 1160 cm^{-1} may also belong to quartz. The characteristic peaks of hematite at 226, 245, 295, 412, 613, 1321 cm^{-1} as shown on Fig. 3 are absent. Peaks are at 632 and 1028 cm^{-1}. They cannot belong to magnetite nor to goethite, which do not show Raman shifts at these wavenumbers. In addition, magnetite may transform into hematite when illuminated with an increased laser power from 0.3 mW to 3 mW following local heating of the sample (Nasdala et al. 2004, p.296; de Faria and Lopes 2007). On the basis of these two reports, the 14 mW laser power used here may provide enough local heat for the oxidation of magnetite into hematite. Therefore, the 632 and 1028 cm^{-1} peaks do not belong to hematite nor magnetite nor goethite. It does not belong either to the epoxy resin that was used to mount the thin section on the glass slide since the characteristic peaks are absent (Fig. 12).
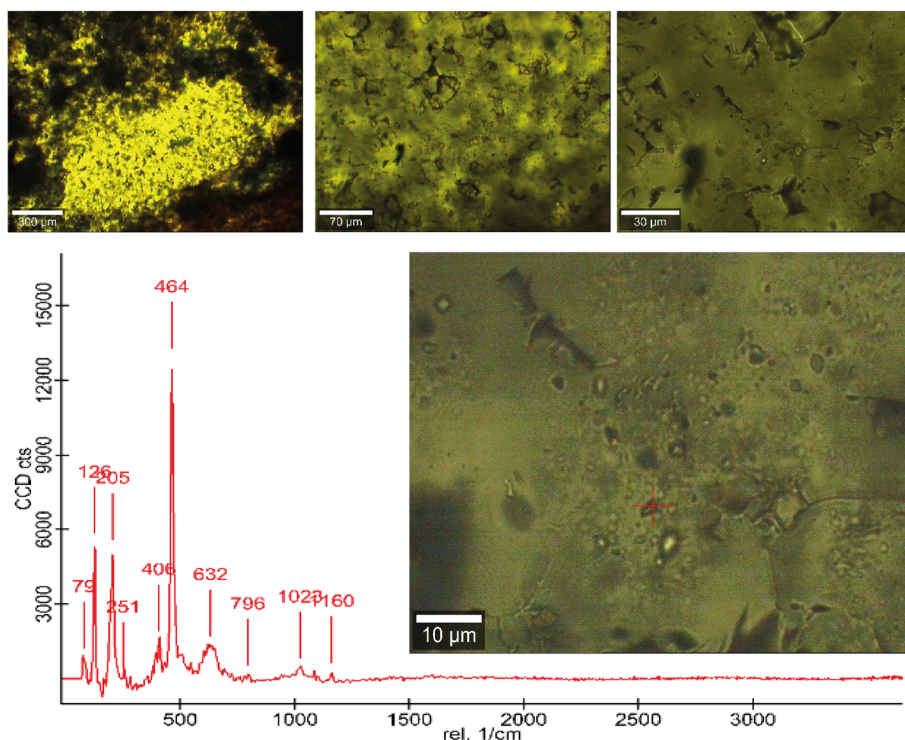

Fig. 11 The quartz grain of the Buck Reef chert BARB3_23B shown on Figs. 2, 9 and 10, observed optically with four different magnifications and a Raman spectrum taken at the position of the red cross. The characteristic peaks of quartz are observed at 126, 205, 464 cm^{-1}. Hematite is absent. The peaks at 632 and 1028 cm^{-1} may belong to greenalite. 532 nm laser, 14 mW laser power at the objective, acquisition time 300 s, WITec Alpha500RA, CBM, CNRS, Orléans
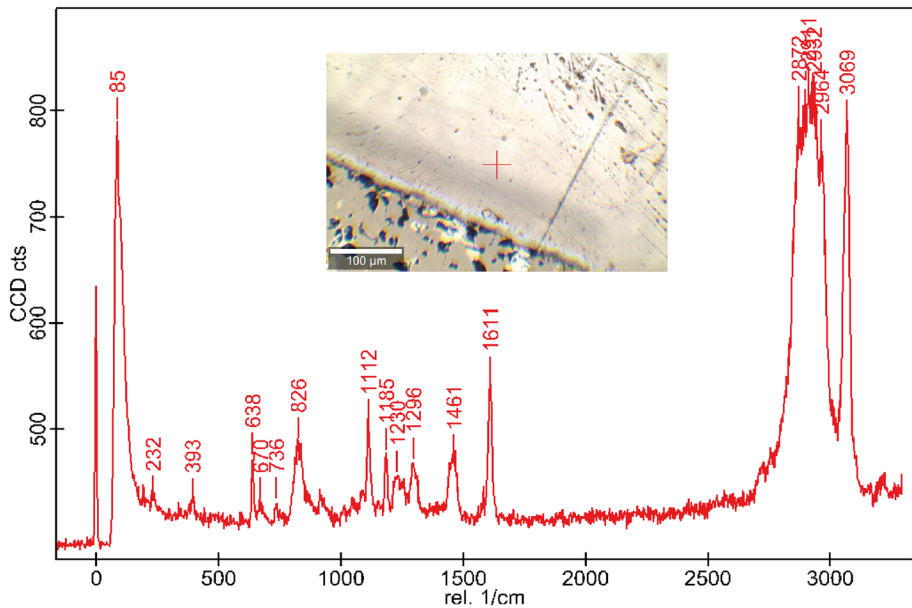
Fig. 12 Raman spectrum of the resin glue on the Buck Reef Chert BARB3_23B thin section. The insert shows an optical image with the red cross at the position of the laser irradiation. 532 nm laser, objective 20x (N 0,75), laser power set to 10 mW and not measured at the sample, acquisition time 10×5 s, detection grating 600 grooves/mm, WITec Alpha300R CY Cergy Paris. The spectrum is analyzed and displayed with no smoothing nor background correction

The 632 and 1028 cm^{-1} peaks seem to correspond to three of the four wide peaks shown at 416, 507, 628 and 1025 cm^{-1} in the Carrière thesis (2017, p.244 Fig. 4) for greenalite from La Union, Murcia, Spain, purchased from Excalibur. The 507 cm^{-1} peak may appear as a wide foot on the BRC 464 cm^{-1} peak of quartz. The Carrière spectrum was recorded with an Invia Renishaw spectrometer equipped with a 532 nm laser, a grating of 2400 grooves/mm and a spectral resolution of 2 cm^{-1}. The BARB3_23B BRC spectrum was recorded with a 532 nm laser, a grating of 600 grooves/mm and a spectral resolution of 4 cm^{-1}. Both spectra show wide lines: the full width at half maximum, FWHM, of the Carrière 628 cm^{-1} peak is~67 cm^{-1}, and the FWHM of the BRC 632 cm^{-1} peak is~65 cm^{-1} (Fig. 11). A Raman spectrum of greenalite is also presented in the Hinz thesis (2018, p.16 Fig. 3). Peaks appear approximately at the same positions as those reported by Carrière:~415 cm^{-1},~501 cm^{-1},~637 cm^{-1} (wide) and~1025 cm^{-1} (wide). They were recorded with a Horiba LabRAM HR Evolution spectrometer equipped with a 532 nm laser.

As shown by Guggenheim and Eggleton (1998) the structures of greenalite $Fe^{II}_3Si_2O_5(OH)_4$ and caryopilite $Mn^{II}_3Si_2O_5(OH)_4$ contain islands of tetrahedral sheets. Both are modulated 1:1 phyllosilicates with Fe and Mn occupying octahedral sites of trioctahedral sheets. The Raman spectrum of caryopilite (RRUFF database at 532 nm) is composed of one~58 cm^{-1} wide peak at~630 cm^{-1} and three peaks at~417,~509 and~1026 cm^{-1}. The caryopilite spectrum is equivalent to the greenalite spectra of (Carrière 2017, Fig. 4) and (Hinz 2018, Fig. 3).

The~1028 cm^{-1} peak is in the 800–1200 cm^{-1} region that has been *"associated with silicon-oxygen stretching vibrations of tetrahedral silicate units"*. The 1200 cm^{-1} peak of

silicate glass corresponds to *"asymmetric stretching within a fully-polymerized tetrahedral silicate network"*, and the 1100–1050 cm^{-1}, 1000–950 cm^{-1}, 900 cm^{-1}, and 850 cm^{-1} peaks correspond to the *"symmetric stretching vibrations of silicate tetrahedra with respectively one, two, three and four nonbridging oxygens* (McMillan 1984a, b; Fu et al. 2017). The Guggenheim structure of greenalite composed of triangular islands that are constructed with three hexagons of six SiO_4 tetrahedra (Guggenheim and Eggleton 1998 Fig. 8) leads to SiO_4 tetrahedra with one or two nonbridging oxygen atoms. The Buck Reef ~ 1028 cm^{-1} may therefore correspond to the symmetric stretching vibration of the silicon-nonbridging oxygen in the silicate tetrahedra of such triangular assemblages.

The intense and wide peak at 632 cm^{-1} belongs to the region 400–700 cm^{-1} which *"has been associated with the presence of inter-tetrahedral Si–O-Si linkages."* (McMillan 1984a, b; Fu et al. 2017). The large FWHM arising from various Si–O-Si angles that characterizes noncrystalline silicates may correspond to the structure of greenalite in islands of tetrahedral sheets.

I propose that the peaks at 632 and 1028 cm^{-1} may be related to the presence of greenalite $Fe^{2+}_3Si_2O_5(OH)_4$ or perhaps $(Fe^{2+}_3Fe^{3+}_2)Si_2O_5(OH)_4$. The present Raman spectroscopy identification of greenalite inside a quartz grain from a sample drilled in the 3.416 Ga Buck Reef chert, Barberton Greenstone Belt, South Africa, complements the earlier assignments of this mineral inside a sample from a core drilled in the 3.46 Ga Marble Bar, Pilbara Craton, Australia (Rasmussen et al. 2014). B Rasmussen identified greenalite with quantitative analysis by scanning electron microscopy—electron dispersive spectrometry (SEM–EDS) conducted on "*fibrous sprays*". The Rasmussen's Fig. 6 shows clusters of greenalite inclusions. The same kind of clusters occurs in the BRC BARB3_23B optical images, produced with the objective 100x and shown in Fig. 11 (10 μm bar). Spherical and cylindrical entities appear grouped within quartz and surrounded by quartz devoid of these entities. The few cylindrical tubes occur with identical sizes of ~ 3 μm long and ~ 1 μm wide and are comparable to the numerous Rasmussen's "*fibers and laths*" of 5 μm long and < 1 μm wide (Rasmussen Fig. 6F, G). Identical images were obtained with a sample located at 288.23 m inside the drill core ABDP9 from a BIF of the Bee Gorge member, Wittenoom formation, of the 2.63–2.45 Ga Hamersley Group in the Mount Bruce Supergroup, Australia (Rasmussen et al. 2015). Greenalite was identified from a 0.72 nm spacing measurement between lattice fringes in a high-resolution transmission electron microscopy (HRTEM) image of the mineral (001) plane. HRTEM and SAED, selected area electron diffraction, conducted on a section located between 327.11 and 327.32 m in the drill core GKF01, from the Upper Nauga Formation of the 2.59–2.46 Ga Campbellrand Subgroup, Griqualand West, Transvaal Supergroup, Kaapvaal Craton, South Africa (Rasmussen et al. 2017), produced d-spacing values closely matching the d-spacing values of greenalite published in (Guggenheim et al. 1982). Greenalite was previously observed in iron formations (Klein 1974; Klein and Bricker 1977). C Klein conducted petrographic and quantitative electron probe microanalysis (EPMA) on drilled samples of the 1.88 Ga Sokoman Formation, western edge of the Labrador Trough in the Canadian shield, and identified oolite granules of greenalite, through chemical composition and textural analysis.

Clusters of fibers, of ~ 500 nm and less in size, with identical morphologies appear grouped inside carbon envelopes in the carbonaceous matter of the 1.88 Ga Gunflint chert formation (Lepot et al. 2017 Suppl Fig. 6g). They are grouped in a quartz matrix and surrounded by quartz devoid of these entities. The difference with Rasmussen nanoparticles is

the carbon sphere which appears to enclose the nanoparticles that are assigned to greenalite and siderite. Gunflint greenalite was shown to be composed of 4.5% Fe^{3+}/Fe_{total} (Lepot et al. 2017 Suppl Fig. 15e). The Raman spectra of 1.88 Ga Gunflint carbon show a D band, three times wider than the 3.416 Ga Buck Reef (Bourbin et al. 2012) and is characteristic of a low greenschist facies with peak temperatures of 200° and 250 °C (Beyssac and Lazzeri 2012 Fig. 8; Buseck and Beyssac 2014 Fig. 5).

Fe^{III}-greenalite was also observed with synchrotron transmission X-ray microscopy applied on the 2.5 Ga samples of the drill holes ABDP9 (Aus.) and GKF (Sth Afr.). Following the protocol outlined in Bourdelle et al. (2013) Fe^{III}/Fe_{total} maps were produced (Johnson et al. 2018 Fig. 2). Low levels of Fe^{III} were observed especially in ABDP9-219 m. Johnson et al. concluded that "*greenalite was dominantly Fe(II) with 10–20% Fe(III)"* and that *"the absence of a spatially coherent redox distribution suggests that this Fe(III) was an original component of the greenalite rather than oxidized by a secondary fluid front"*.

No quantitative experiment of Fe^{III} in the micrograins assigned to greenalite has been conducted in the present study. The possible presence of Fe^{III}-greenalite in BARB3_23B is based on the Raman wavelength at ∼3620 cm^{-1} which can arise from the presence of Fe^{3+} in octahedral sites as described in the next subsection on " *Observation of NaOH and Fe^{III}-greenalite"*. It is also based on morphologies comparison with geological objects containing Fe^{III}-greenalite as described in the above paragraphs. An explanation for the synthesis of Fe^{III}-greenalite in such objects and in BARB3_23B is given by the proposed hypothesis on the interaction of ferrous silicates, such as fayalite and ferrosilite, with anoxic, abiotic, strongly alkaline high-subcritical water. The dissolution of fayalite in high-subcritical water produces Fe^{2+} ions that are oxidized by water with 700–600 kg/m^3 densities, at 300–350 °C, 10–25 (and up) MPa, and pH 9.5–14. The presence of greenalite or Fe^{III}-greenalite in an environment of only quartz, hematite and siderite leads to the conclusion that the mineral greenalite was formed 3.4 Ga ago and not at a later stage.

Results. Water, Methane, Sodium Hydroxide, Fe^{III}-greenalite Inside Quartz Cavities

Strongly basic water, methane and possibly Fe^{III}-greenalite are observed inside quartz cavities.

Water

Water is observed inside quartz cavities, ususally named fluid inclusions.

A preliminary search for fluid inclusions in the BARB3_23B thin section of the drilled sample in the Buck Reef chert was conducted at the LGCgE, Lille, on March 10th, 2020. Only five fluid inclusions were recognized on the entire thin section. They are primary and constructed within the quartz crystal. They belong neither to veins nor fissures. Figure 13 shows one fluid inclusion which is positioned exactly at the center of the image. Its content observed by Raman spectroscopy at 532 nm displays a broad band with two maxima at ∼3208 cm^{-1} and ∼3431 cm^{-1}, and two sharp peaks at ∼3617 cm^{-1} and ∼3620 cm^{-1}. Following the positive preliminary results obtained in 2020, a more detailed search for fluid inclusions was conducted in 2021, between August 12th and 20th. Figure 14 displays optical images of the quartz grain that was investigated. One image is rotated for
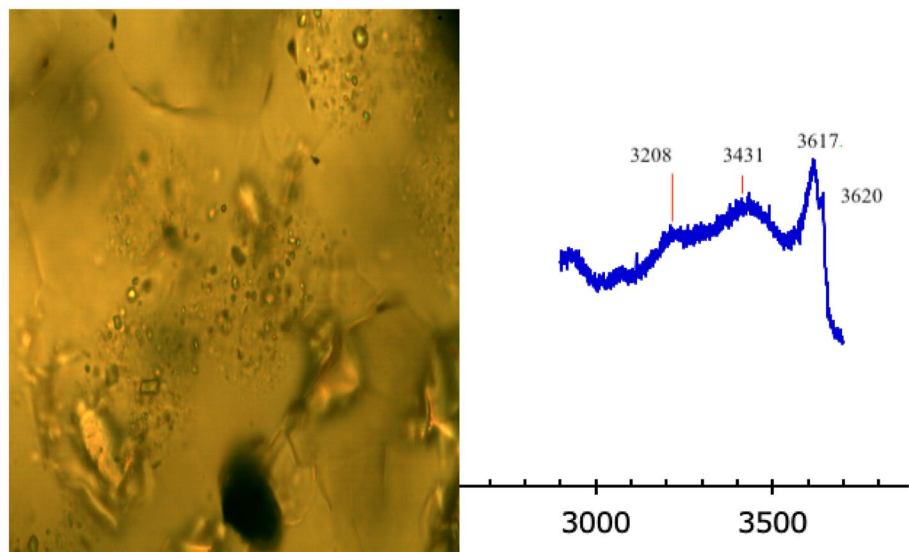
Fig. 13 One fluid inclusion of the Buck Reef chert BARB3_23B positioned exactly at the center of the image, and its content recorded with the laser beam pointing inside the inclusion. Liquid water peaks at ~ 3208 and 3431 cm^{-1}. The peaks at 3617 and 3620 cm^{-1} belong either to NaOH or greenalite. 532 nm laser, Horiba Jobin Yvon HR800, thin section, LGCgE, Lille, March 10th, 2020

recognition with the quartz grain of Figs. 2, 9, 10, and 11. A circle surrounds the studied fluid inclusion. Figure 15 displays the Raman spectra recorded inside the fluid inclusion of Fig. 14. The four peaks at ~ 3208 cm^{-1}, ~ 3431 cm^{-1}, ~ 3617 cm^{-1} and ~ 3620 cm^{-1} are recognized. The peaks at ~ 3208 and ~ 3431 cm^{-1} correspond to the 3200 and 3400 cm^{-1} bands of liquid water as described in (Rice and Sceats 1981 Fig. 2; Shaffer 1998 Figs. 5 and 7; Pastorczak et al. 2008; Dubois et al. 2010 Table 4). Several authors have processed the spectrum of liquid water in various ways, including Gaussian and Lorentzian curves, water stretching vibration peaks, and the effects of dissolved ions and hydrogen bonding (Carey 1996; Carey and Korenowsky 1998; Baumgartner and Bakker 2009; Li et al. 2018; Ghosh et al. 2023, and refs therein).

The BARB3_23B peaks at ~ 3208 cm^{-1} and ~ 3431 cm^{-1} correspond to the OH stretching vibrations of liquid water. The ~ 3617 cm^{-1} and ~ 3620 cm^{-1} sharp peaks may be assigned to NaOH and greenalite, as studied in the next paragraph.

NaOH and Fe^{III}-greenalite

Sodium hydroxide and Fe^{III}-greenalite may be present inside quartz cavities.

The peaks at 3617 and 3620 cm^{-1} of Figs. 13 and 15 may correspond to the stretching mode of vibration of the OH group of sodium hydroxide when NaOH is added to pure water. Shaffer (1998 Figs. 8 and 14) reports the change in the Raman profile of water when sodium hydroxide is added. One sharp peak appears at ~ 3600 cm^{-1}. De Oliveira et al. (2021 Fig. 1A) likewise reports the 514.5 nm Raman spectra of NaOH solutions recorded with a laser power of 20 mW at the sample. Their 2 M NaOH profile resembles the Shaffer's
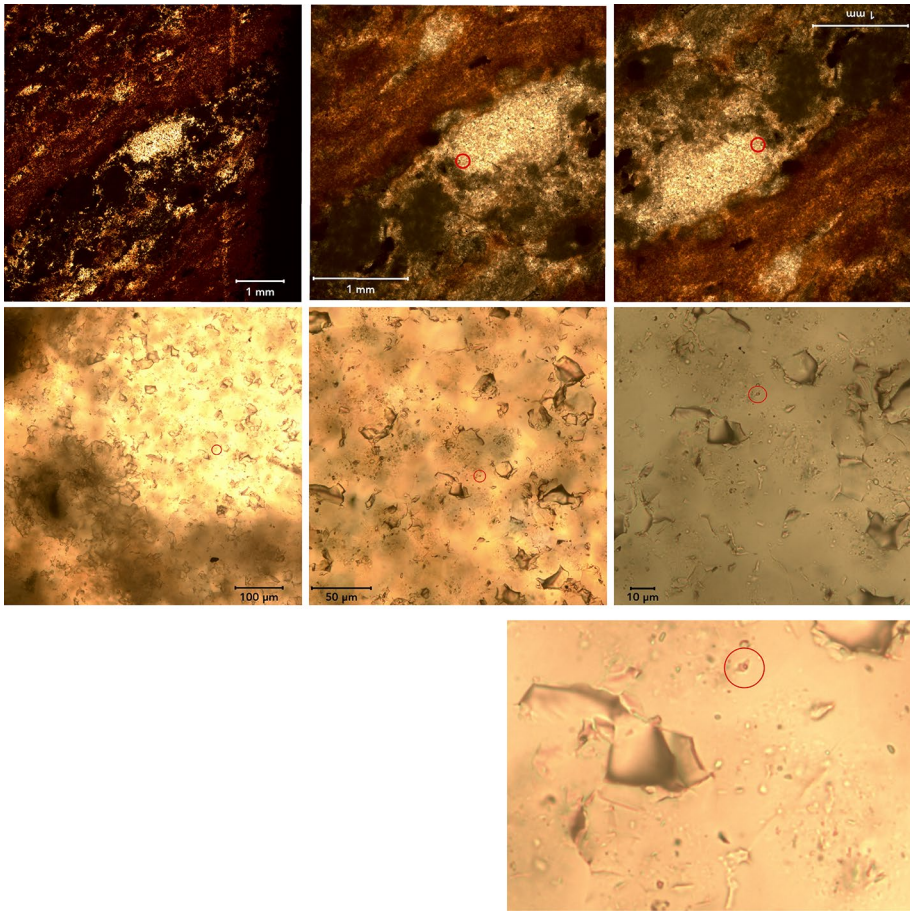
Fig. 14 Optical search for fluid inclusions. Objectives 2x (1 mm bar), 4x (100 μm), 20x (50 μm), 50x (10 μm), numerical zoom. The 3rd "1 mm" image is rotated for recognition of the quartz grain on Figs. 9, 10 and 11. Circles surround the studied 3.25 μm fluid inclusion. Buck Reef BARB3_23B thin section, LGCgE, Lille, August 2021

profile located in between 5 and 10 w/o, with the peak at ~ 3600 cm^{-1} starting to grow. This correspondence seems correct since a 2 M solution of NaOH (molar mass of 40 g/mole) contains 2 mol of NaOH per liter of water, which is 80 g NaOH/L water, or 8% weight NaOH/weight water. The BARB3_23B profiles of Figs. 13 and 15 resemble the Shaffer curve labelled 30 w/o. Considering that 30 w/o means 30% w/w NaOH/water, the following simple calculation can be made: The solution contains 300 g NaOH per 1000 g water, which is 7.5 mol NaOH per liter water or per 55.55 mol of water. In other words, an NaOH aqueous solution 7.5 M, at a concentration $\sim 1{:}7$ (1 mol NaOH per 7.4 mol water) displays a Raman profile that is equivalent to that of the BARB3_23B water.

$$p(OH) = -\log_{10}(OH^-) = -\log_{10}(7.5) = -0.875 \qquad p(H) = 14 - p(OH) = 14,875$$

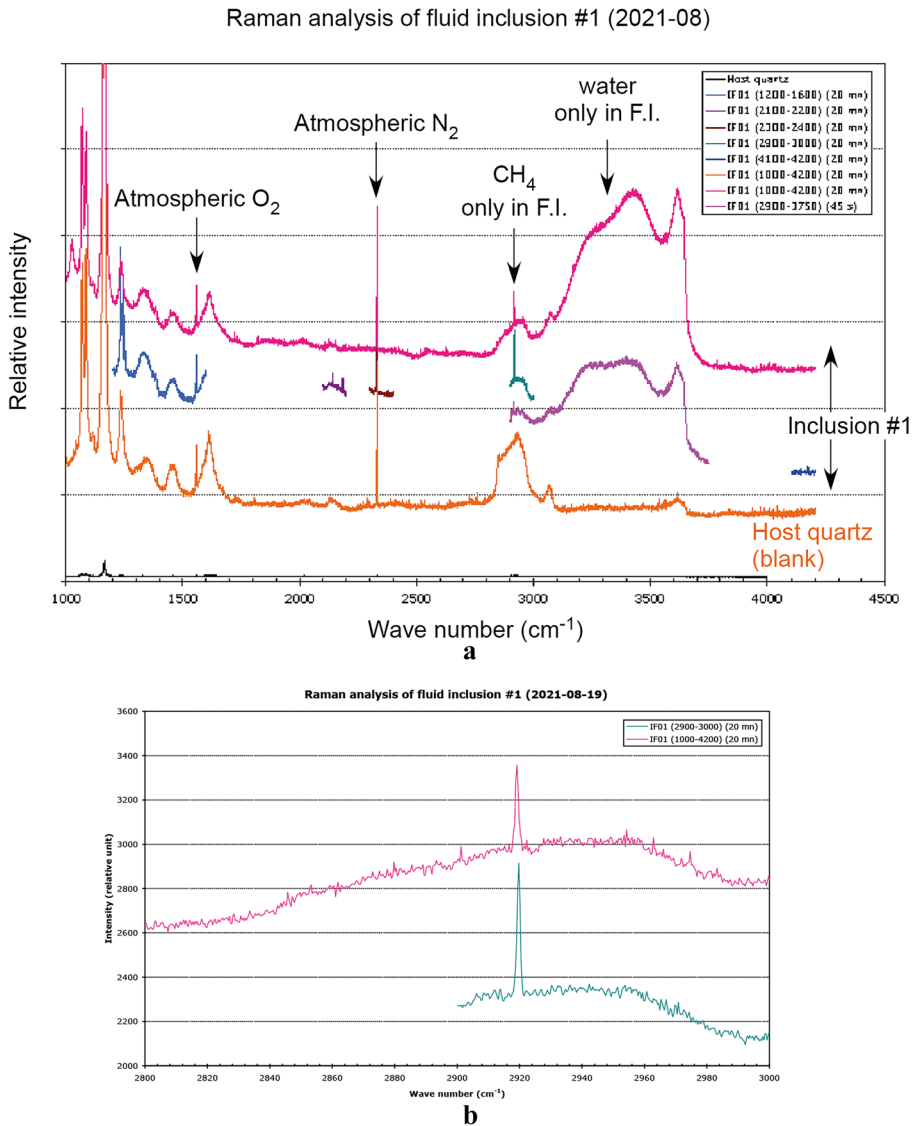Raman analysis of fluid inclusion #1 (2021-08)

a

b

Fig. 15 Raman spectra recorded inside the fluid inclusion and the host quartz that are shown on Fig. 14. The sharp peak at 2917 cm.$^{-1}$ is assigned to methane. 532 nm laser, Horiba Jobin Yvon HR800, Buck Reef BARB3_23B thin section, LGCgE, Lille, August 2021

The value of pH approaches 15. The solution is strongly basic. This result is confirmed by the observation of the 514.5 nm Raman profile reported in (Corridoni et al. 2007 Fig. 2) where a 1:6 NaOH aqueous solution, 1 solute per 6 water molecules, shows a *"sharp OH$^-$ stretching band at 3620 cm^{-1}"*, which peaks with an intensity corresponding to the BARB3_23B. The equivalence in Raman profiles of the BARB3_23B water and of a strongly basic pH solution can likewise be recognized in (Stefanski et al. 2018 Figs. 1 and 10, Table 3) where a 5.5 M NaOH aqueous solution is followed by Raman spectroscopy

during increases in temperature and pressure. The profiles at 21 °C, 0.1 MPa and 300 °C, 8 MPa display sharp peaks at ~3615 cm^{-1} and ~3622 cm^{-1} respectively.

Another interpretation of the ~3620 cm^{-1} peak takes its origin within the minerals. The Raman spectrum of kaolinite $Al^{III}_2Si_2O_5(OH)_4$ displays a sharp and strong peak at 3620 cm^{-1}, without specification of the laser wavelength, in (Horvath et al. 2010) and at 3622 cm^{-1} in (Wang et al. 2015 Figs. 3c, 5) with a 532 nm laser, while the Raman spectrum of chrysotile $Mg^{II}_3Si_2O_5(OH)_4$ does not (Wang et al. 2015 Fig. 6). These two phyllosilicates differ according to the cation arrangement in octahedral sites as described in (Wang et al. 2015): *"Dioctahedral phyllosilicates have two-thirds of sites in the octahedral (Oc) layer filled by Al^{3+} or Fe^{3+} cations. Trioctahedral phyllosilicates have all three sites in the Oc layer filled by Mg^{2+}, Fe^{2+}, and other divalent cations"*. The 3620 cm^{-1} peak is assigned to the stretching mode of the inner hydroxyl group (Horvath et al. 2010 Figs. 2, 3). The phyllosilicate Fe^{III}-greenalite $(Fe^{II}Fe^{III})_{3-2}Si_2O_5(OH)_4$ with both divalent and trivalent cations, if present, may be at the origin of the ~3620 cm^{-1} peak, because of the presence of Fe^{3+} in octahedral sites. The above section on the observation of greenalite assigns the peaks at ~632 cm^{-1} and ~1028 cm^{-1} to greenalite. The Raman spectrum of the inclusion displayed on Fig. 15 shows a weak peak at ~1028 cm^{-1} which is absent in the spectrum of the host quartz. Fe^{III}-greenalite may be present inside the inclusion.

The ~1028 cm^{-1} peak and the ~3620 cm^{-1} peak may indicate the presence of Fe^{III}-greenalite inside the inclusion. The ~3617 cm^{-1} and ~3620 cm^{-1} peaks may indicate the presence of NaOH at high concentration leading to a strong basic solution at pH ~15 inside the inclusion.

Methane

Methane is observed inside quartz cavities.

Figure 15 shows peaks of atmospheric O_2 and N_2. The peak of gaseous methane at 2917 cm^{-1} (Raman shift described in Frezzotti et al. 2012; Lacroix et al. 2014 Fig. 9) is present only in the Raman spectrum of the inclusion. Methane is unambiguously present inside the fluid inclusion.

Conclusion on the Content of the Fluid Inclusions

The quartz cavities or fluid inclusions of the BARB3_23B BIF drilled inside the Buck Reef chert show unambiguously liquid water and gaseous methane. The ~3617 cm^{-1} and ~3620 cm^{-1} peaks may be assigned to the stretching mode of vibration of the OH group of a sodium hydroxide aqueous solution which is extremely basic, with pH ~15. The ~3620 cm^{-1} peak may also be assigned to the stretching vibrations of the OH groups that are octahedrally linked to the Fe^{III} cations in Fe^{III}-greenalite. This assignment may be confirmed by the presence of a greenalite peak at ~1028 cm^{-1} in the spectrum of the inclusion. The two ~3617 cm^{-1} and ~3620 cm^{-1} peaks may represent superposed bands of both NaOH and Fe^{III}-greenalite, with a high overlapping of the NaOH component, leading to the conclusion that Archean water was strongly basic (pH 15) at the location where the minerals of the Buck Reef BIF formed. This interpretation would be a confirmation of the formation of the minerals, methane and carbon as presented in Fig. 16.
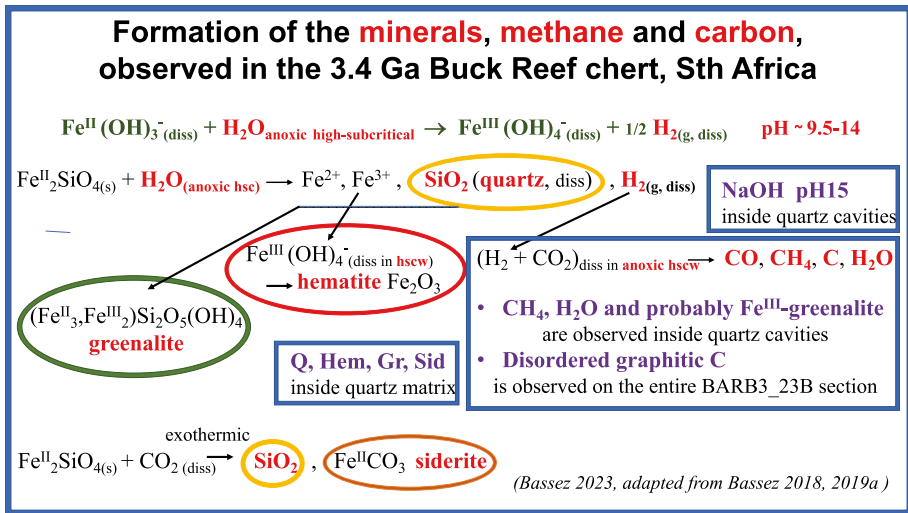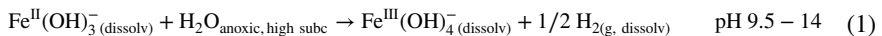
Fig. 16 Proposed chemical formation of the minerals quartz, hematite, greenalite, siderite, and of methane and disordered graphitic carbon, observed in the thin section 23B of the sample located between 471.26 m and 471.48 m inside the BARB3 core, drilled in the 3.4 Ga Buck Reef chert, South Africa. red: predicted by the theory; violet: observed

Origins of the BARB3_23B Minerals, Methane, Disordered Graphitic Carbon and Molecules of Life

Origin of the BARB3_23B Minerals

The minerals of the Buck Reef BARB3_23B sample may have been synthesized in anoxic strongly basic water in the high subcritical domain, at 300°-350 °C, 10–50 MPa, pH 9 to 15, without the presence of UV light or microorganisms.

Figure 16 summarizes the results of the analyses of the BARB3_23B section of the Buck Reef chert and proposes a schema for the formation of the minerals quartz, hematite, greenalite, siderite, and for methane and disordered graphitic carbon. It is adapted to the present observations from (Bassez 2018, 2019a). The basis of the diagram is the chemical Eq. (1) which has been proposed since (Bassez 2013) for the oxidation of ferrous iron in anoxic and strongly alkaline high subcritical (hsubc) water at temperatures of 300°-350 °C and pressures of 10–50 MPa.

$$Fe^{II}(OH)_{3\ (dissolv)}^- + H_2O_{anoxic,\ high\ subc} \rightarrow Fe^{III}(OH)_{4\ (dissolv)}^- + 1/2\ H_{2(g,\ dissolv)} \qquad pH\ 9.5-14 \quad (1)$$

It is plausible that this alkaline anoxic oxidation of ferrous iron can proceed in supercritical water. However, E-pH diagrams cannot currently be drawn for T and P above the critical point because experimental results are lacking for such water structures. Fayalite and ferrosilite are the best candidates to produce the observed minerals. It is hypothesized that fayalite dissolves in high subcritical water, i.e. water approaching the critical point from below, to produce silica and Fe^{2+} ions, which are oxidized into Fe^{3+} with the emission of H_2. The formed ferric tetrahydroxide anion is in fact the anion form of hydrated goethite, which can dehydrate into hematite.

$$Fe^{2+} + H_2O_{hsc} \rightarrow Fe^{II}(OH)_3^- \rightarrow Fe^{III}(OH)_4^- = FeOOH(H_2O)OH^- \rightarrow Fe_2O_3 \qquad (2)$$
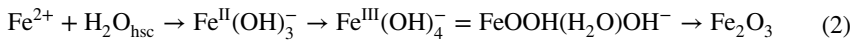
The dissolution of fayalite in anoxic alkaline high subcritical water has not yet been proven in the laboratory. Experiments are under preparation. This dissolution is predictable, since the solubility of silica, which is known to be higher in hsubc water than at ambient temperature, would drive the dissolution of fayalite towards the formation of Fe^{2+} ions. In addition, silica adsorbs onto hematite as described in (Bassez 2018, p 294 and refs therein), leading to a decrease in the silica content of the solution when hematite precipitates. Further dissolution of fayalite (and ferrosilite) is then induced until silica saturation.

In 2016, was reported an experiment conducted on dissolved Fe^{2+} mixed with SiO_2 in anoxic water at 25 °C (Tosca et al. 2016). A Fe^{II}-silica gel that transformed into Fe^{II}-greenalite was observed. The nucleation of greenalite at pH 9 started at much lower contents of Fe^{2+} than at pH 7. This experiment is a proof that greenalite, $Fe^{II}_3Si_2O_5(OH)_4$, can nucleate in alkaline anoxic aqueous solutions containing Fe^{2+}. In alkaline hsubc water, the Fe^{2+} ions oxidize, and Fe^{II}-greenalite, $Fe^{II}_3Si_2O_5(OH)_4$, can transform into Fe^{III}-greenalite, $(Fe^{II}_3Fe^{III}_2) Si_2O_5(OH)_4$. The mineral Fe^{III}-greenalite was observed in the 1.88 Ga Gunflint chert (Lepot et al. 2017) and the ~ 2.5 Ga BIFs of Western Australia and South Africa (Johnson et al. 2018). Greenalite is tentatively identified in the present study of the 3.4 Ga Buck Reef chert, following the assignment of two Raman peaks (section on greenalite), and even Fe^{III} -greenalite with the assignment of a peak to vibrations of OH groups which can be octahedrally linked to Fe^{3+} cations (section on greenalite inside quartz cavities).

The carbonations of fayalite and ferrosilite are exothermic (Bassez 2013, 2015, 2017a, b). The temperatures of hsubc water are therefore not required for the formation of siderite $FeCO_3$. They are nonetheless required for the decomposition of siderite into magnetite, carbon dioxide CO_2, carbon C, and hydrogen H_2, as shown in experiments conducted at 300 °C / 50 MPa by (Milesi et al. 2015) and at 455°- 465 °C / 50 - 200 MPa pressure of $CO_2 + CO$ by (French and Rosenberg 1965). The Raman observations of the BARB3_23B section of the Buck Reef chert do not show any magnetite. The deposition of carbon cannot come from a decomposition of siderite, or the magnetite has been submitted to higher temperatures and transformed into hematite.

Origin of the BARB3_23B Methane and Disordered Graphitic Carbon

The methane of the BARB3_23B sample may have been formed locally when dissolved CO_2 interacted with the H_2 emitted during the oxidation of Fe^{2+} by high subcritical water. The disordered graphitic carbon may have been deposited from the anoxic methane-rich fluid.

Holloway's (1984, ternary diagram of the C, O, H thermodynamic system, shows that in anoxic water at T and P in the high subcritical domain, 300 °C, 100 MPa, methane is at equilibrium with graphitic carbon and a small amount of water. *"The fluid compositions coexisting with graphite can be treated as two binary systems: CO_2-H_2O and CH_4-H_2O, for any T < 400 °C. Calculations show that this behavior is similar for any P from 300 to at least 10 000 bar."* The anoxic domain of Holloway's diagram is represented by a narrow area along the C-H line where graphite is in equilibrium with methane and very little water. Experimental confirmations of the formation of CO and CH_4 were reported earlier for gaseous mixtures of CO_2 and H_2 (Sabatier and Senderens 1902; Chen et al. 2000) and for mixtures of gaseous CO_2 and H_2 dissolved in high subcritical water at 250°-300 °C and 25 MPa with magnetite as catalyst (Fu

and Seyfried 2009) as described in (Bassez 2018). In geological terrains, when anoxic CO_2-rich water encounters sites filled with H_2, CO_2 can transform into CO and then CH_4. Indeed, Archean Earth was anoxic, with surface O_2 levels that are proposed to be $< 10^{-6}$ PAL, present atmospheric level (Catling and Zahnle 2020). When Archean CO_2-rich water containing no dissolved O_2 encountered blocks of ferrous rocks, at temperatures and pressures of high subcritical water and at high pH, the CO_2 can react with the H_2 produced during the oxidation of Fe^{2+} and transform into CO and CH_4. Upon Holloway's diagram, the CH_4 must be at equilibrium with graphitic carbon. The very reactive CO can bind to some graphene layers forming what is represented by the general term disordered graphite. This interpretation illustrates the evolution of the bulk composition of the CO_2-rich water towards a CH_4-rich water during an experiment diffusing H_2 into an initially pure CO_2 fluid inclusion in quartz (Pasteris and Chou 1998 Fig. 6, line from CO_2 to H in the Holloway's C–O–H system; Ziegenbein and Johannes 1990). Pasteris and Chou concluded: *"Whereas graphite formed by* in situ *metamorphism* (of organic matter) *shows a distinct increase in crystallinity with increasing grade, the correlation is not so simple for fluid-deposited graphite. For fluid-deposited graphite, not only temperature, but also gas fugacities and total pressure affect the measured crystallographic values…We determined that the precipitation of more crystalline graphite is favored by lower fH₂…"* Based on Pasteris and Chou, the precipitated graphite may be plus or minus ordered, depending on the amount of H_2, and I add upon the amount of CO produced.

Luque et al. (1998) described the similarities and differences between metamorphic graphite (formed in situ from organic matter) and fluid-deposited graphite. They noticed several morphologies for deposited graphite *"…medium- to coarse-grained flakes or needles* (resembling) *high-grade metamorphic graphite… spherulitic aggregates displaying radial arrays…nodules composed of coarse crystals surrounded by thin flakes…"* (Luque et al. 1998 p.477 and refs therein). As described in (Maj and Kocemba 2018), carbon filaments, in the form of carbon nanotubes and nanofibres, and amorphous carbon are deposited on the surface of nanocrystalline iron catalysts, during thermal decomposition of methane in a quartz reactor, 6 mm in diameter. Nanocrystalline iron catalysts were obtained by fusion of magnetite Fe_3O_4 or wüstite FeO, with small amounts of the oxides Al_2O_3, CaO, K_2O, and Co_3O_4. Methane decomposition was tested between 200° and 700 °C. The best catalyst activity was observed at 700 °C, with a process of methane decomposition according to the reaction: $CH_4 \leftrightarrow C + 2H_2$. The Buck Reef BARB3_23B BIF has been submitted to temperatures of ~ 335 °C, as shown in the section on *"carbon matter and temperature"* of the supplementary file. At this temperature, methane decomposition may occur but with slower kinetics.

Another path for graphite deposition is the transformation of siderite either by decomposition or by reaction with high subcritical water. Experiments indicate that siderite decomposed to magnetite, graphite, CO_2 and CO, at 455°- 465 °C and 50–200 MPa pressure of CO_2 plus CO (French and Rosenberg 1965). Disordered graphite was proposed to precipitate from gaseous CO. More recent experiments conducted on siderite dissolution at 200°-300 °C and 50 MPa, which are T and P values located in the high subcritical domain of water, show the formation of magnetite, CO_2, H_2, CH_4, and condensed carbon phases (Milesi et al. 2015 and refs therein). With dry siderite, there was no decomposition of siderite. *"The carbon matter which encapsulates magnetite grains is made of a stack of layers, presumably short graphene units ".* These two above formations of disordered graphite, starting from siderite, cannot apply to the BARB3_23B Buck Reef carbon since the Raman spectra show only hematite and no magnetite.

Liquid water and gaseous methane are present in the two studied fluid inclusions of Buck Reef, together with either NaOH or greenalite, or both. At 300°-350 °C and 25 MPa, water is in the high subcritical domain with densities of 700 - 600 kg/m^3 (Cook and Olive 2012), and methane is supercritical with much lower densities of approximately 65 kg/m^3. Inside quartz cavities, methane was enclosed, could not escape and remains today as a remnant of the Archean anoxic water. Outside the cavities, methane could ascend, leaving a fluid supersaturated in carbon that was deposited as disordered graphitic carbon. This proposition is supported, as described in the first paragraph of the present section, by the Holloway's C-O–H 1984 diagram and by the 1998 extension made by Pasteris and Chou considering H$_2$ fugacities, and by my proposition in the present article to consider the possibility of chemical adsorption of CO on the graphene layers.

Arguments against the carbon deposition hypothesis may be provided by articles reporting that fluid-deposited graphite is usually well-ordered (Luque et al. 2009, Lepland et al. 2011 Table 1 (R1 = I$_D$/I$_G$ low), Parnell et al. 2021 Fig. 4). *"The structural data obtained by means of XRD, Raman spectroscopy, and HRTEM indicate that natural graphite precipitated from fluids is fairly homogeneous (unlike metamorphic graphite), that is, there are no large fluctuations in the "crystallinity" of a given sample"* (Luque et al. 1998 p.488, 490 and refs therein). Nonetheless, Luque et al. (2012) noticed that *"graphite precipitated from fluids containing only CH$_4$ are less documented* (than from CO$_2$-rich fluids)*."* And Fig. 3a and c in (Chinnasamy and Mishra 2017), reporting Raman spectra that are recorded from the Jonnagiri Archean greenstone belt, show that the spectrum of the (CH$_4$ + CO$_2$) inclusion displays two peaks of equivalent intensity, characteristic of disordered graphitic carbon, at ~ 1351 and ~ 1601 cm^{-1}. The spectrum of the (CH$_4$ rich with little CO$_2$) inclusion (Fig. 3c) displays these two peaks on a long range of wavelengths. A shorter range would specify the carbon peaks and most probably show that they resemble those of the BARB3_23B carbon matter. The argument of well-ordered deposited graphite would be declined.

Another argument against the carbon deposition hypothesis can arise from the distribution of the carbon matter in the BARB3_23B sample, which appears homogeneous with grains of ~ 4 to ~ 20 μm in size (Figs. 7a, 8a, 9e, 10e). This observation seems to contradict the following description: *"For fluid-deposited graphite occurrences, changes in the carbon content of the fluid (supersaturation) appear to be the most likely factor controlling the different graphite morphologies"* (Barrenechea et al. 2009), with cryptocrystalline and spherulitic aggregates that form under high supersaturation, and flaky crystals that develop under lower supersaturation, as expressed for the Borrowdale Volcanic Group of the upper Ordovician period (~ 450 Ma). The Barrenechea et al. Fig. 4 shows first-order Raman spectra of different graphite morphologies, which display different Raman profiles, either well-ordered or with disordered graphite characteristics. In the case of the BARB3_23B of the Buck Reef BIF, as methane escapes, the remaining fluid should become richer in graphitic carbon and increasingly supersaturated. Based on the Barrenechea et al. description, morphologies the BRC BARB3_23B should change instead of being all identical. However, the studied sample measures 4 cm in length. It may be worthwhile to study the carbon matter of Buck Reef in an extended environment of the sample and proceed to observations at a nanometer scale.

As a conclusion, the Buck Reef BARB3_23B carbon matter shows a homogeneous distribution of aggregates possibly deposited from Archean water, which became methane-rich when encountering the H$_2$ emitted during the oxidation of ferrous iron by alkaline anoxic high subcritical water. The CH$_4$-rich fluid originated from the CO$_2$ dissolved in the Archean anoxic oceanic water which, in the presence of H$_2$, transformed into CO and then CH$_4$ to reach equilibrium with graphitic carbon. The origin of the disordered graphitic carbon, which is present on the entire BARB3_23B thin section, can be the deposition from

a low supersaturated methane-rich anoxic fluid that formed in geological environments of ferrous silicates and strongly basic high subcritical water. An explanation for the deposition of disordered graphitic carbon instead of well-ordered graphite is the presence of the very reactive organic functional group CO, which may attach to the graphene layers.

Origin of Molecules of Life Inside Mineral Cavities

Chiral chemistry may proceed within mineral cavities through the interaction of the synthesized molecules of life with the crystal acting as frontier of the cavity.

Mixtures of CO, H_2, N_2/NH_3 which were heat excited, were demonstrated in the laboratory to lead to molecules of life, such as amino acids and their precursors (Hill and Nuth 2003; Pizzarello 2012). The observation of methane inside quartz cavities of the BARB3_23B sample may be proof that H_2 was present in Archean high subcritical water, transforming CO_2 into CO and CH_4. N_2 was also present in the Archean atmosphere. It has been estimated to be *"≤1 bar (scaled to the modern P_{N2} of 0.79 bar), and possibly as low as 0.5 bar."* (Marty et al. 2013 and refs therein). Amino acids and their precursors could form inside quartz cavities, which are also called fluid inclusions, and are empty spaces without membranes, in which small molecules can concentrate and lead to the synthesis of complex molecules. The synthesis of biological molecules that is made possible because of the H_2 emitted during the hsubc water-ferrous silicates interaction, is called Geobiotropy (Bassez 2016). Since no N_2 has been observed inside the studied fluid inclusions of the BARB3_23B Buck Reef chert, it may be considered that either no amino-acids formed or all the N_2 of the cavity has been consumed to form organic molecules.

Further experiments are envisioned with Atomic Force Microscopy coupled to InfraRed spectroscopy (AFM-IR). Searches for organic molecules of life, such as amino acids, need to be conducted inside fluid inclusions of the Buck Reef chert or other Archean ferric iron formations, because fluid inclusions that are primary formed at the time of the mineral formation. I envisioned a possible synthesis in (Bassez 2003): *"the mixture of the apolar molecules, CH_4, H_2, N_2, H_2O, H_2S and CO_2…could lead to prebiotic synthesis…reactions could occur inside cavities acting as chemical reactors…the deposition occurring at the turbulent interface* (of the chimneys) *between superhot and cold water could create a spongy solid with microcavities and nanochannels…"* This kind of synthesis may bring knowledge on the origin of molecules of life inside Archean minerals that formed during anoxic conditions. Following this idea, we analyzed the content in organic molecules of two serpentinized peridotite rocks that were dredged on the floor of the Ashadze and Logatchev hydrothermal sites in the Mid-Atlantic Ridge (MAR) at a depth of 4080 m and 2970 m below sea level respectively (Bassez et al. 2009). Large enantiomeric excesses of the L-form of amino-acids and long chain *n*-alkanes were identified by GC/MS, gas chromatography/mass spectrometry. The samples were grounded. No distinction could be done between the rock matrix and the cavities. A recent study by (Nan et al. 2021) was conducted on an equivalent rock, a serpentinized harzburgite peridotite dredged on the floor of the Yap Trench, western Pacific Ocean, at a depth of 6413 m. Spectra (their Fig. 3) recorded with AFM-IR and PiFM-IR, Photo-induced Force Microscopy coupled to InfraRed spectroscopy, show CH vibrations present inside ~50 nm pores and 10–20 µm cavities. EDX, energy dispersive X-ray spectroscopy, images show the association of Fe and C. For the three sites, Ashadze, Logatchev and Yap Trench, the rocks were dredged on the floor

of the ocean. We demonstrated that the amino acids observed in Logatchev and Ashadze are from biological origin, probably from modern time biological remains which fell on the surface of the ocean crust while, abiotically synthesized amino-acids were produced during experiments on proton-irradiated mixtures of CO, N_2 and H_2O (Bassez et al. 2012). Infra-red studies of the BARB3_23B ~ 3 μm quartz cavities are required on a nanometer scale. Results would bring knowledge on the presence or not of organic molecules and their potential association with iron minerals, inside the ~ 3 μm inclusions which formed 3.4 Ga ago, at the time of the quartz formation. The synthesis of molecules of life inside rock cavities, that I envisioned in 2003 and conceptualized as Geobiotropy inside mineral cavities called fluid inclusions (Bassez 2016, 2017c, 2018), may thus be verified.

Prebiotic chemistry may proceed inside cores of the cavities and through interactions with the surfaces of the mineral surrounding the cavity. Specific orientations and bonds may form depending on the cavity and mineral geometries, leading to asymmetric carbon atoms and homochirality. Crystallographic arrangements inside minerals such as quartz, amorphous silica, crystallized and amorphous greenalite, siderite, may lead to the synthesis of chiral molecules of life. The SiO_4 tetrahedra of quartz are arranged in helical structures which lead to left- and right-handed trigonal-trapezohedral crystals with specific electrical, optical and magnetic properties. It seems important to study the possible relations between the crystallographic helix structures of quartz and the asymmetric structures of the molecules that can attach to the various quartz crystals. The tetrahedral and octahedral sites of phyllosilicates may also lead to specific orientations. These connections between silicates, carbonates, and molecules of biological interest could contribute to explain why chiral molecules are observed on Earth and in meteorites.

Construction of the Banded Iron Formations

Archean and Neoproterozoic BIFs can be constructed by the ejection of the water mixed with minerals that form inside Fe^{2+}- H_2O reaction chambers.

On the stratigraphic column of the Barberton greenstone belt, drawn by Lowe and Byerly (2020), the BRC is clearly positioned between volcanic rocks: the underlying felsic volcanic and some komatiitic volcanic rocks of the H_6 member of the Hooggenoeg Formation and the overlying younger basaltic volcanic rocks of the Kromberg Formation. The stratigraphic column shows volcanic rocks on a span of 291 million years between 3.547 and 3.256 Ga. It appears quite logical to propose that the construction of the 3.4 Ga BRC belongs to a volcanism event. The same process of formation can most likely be applied to all BIFs, which appear usually intercalated between volcanic rocks.

Figures 17 and 18 propose plausible paths of formation for the minerals of the BRC BARB3_23B section and for the minerals of banded ferruginous cherts. They are drawn for high subcritical water. Complementary images will be drawn later on for supercritical water, after the completion of hydrothermal experiments that are currently under progress. Archean water, percolates inside the crust and the upper mantle, and may interact with blocks of ferrous rocks, while being at the correct pH, T and P for ferrous oxidation to occur. Fe^{2+} ions oxidize into Fe^{3+}, forming $Fe^{III}(OH)_4^-$, which further dehydrate into Fe_2O_3. Dissolved Fe^{2+}, Fe^{3+} and silica assemble into $Fe^{II}Fe^{III}$-greenalite. Oxidation of Fe^{2+} releases H_2, leading to the transformation of CO_2 into CO and then CH_4. The water at the

location of the ferrous rocks becomes a CH_4-rich fluid at equilibrium with graphitic carbon. A second type of interaction occurs between Fe^{2+} ions and carbon dioxide to form quartz and siderite in an exothermic process. Two types of liquid may thus be created in a sort of liquid–liquid fractionation. The blocks of ferrous rocks may act as Fe^{2+}-H_2O_{hsubc} chemical reaction chambers. The ferrous rocks may be fayalite or ferrosilite, or other kind of ferrous iron bearing minerals. Hydrothermal experiments are currently in progress to follow the oxidation of strongly alkaline water as a function of temperature below and above the critical point of water. They will determine if supercritical water can oxidize Fe^{2+} and specify the possible depths of the chemical interaction chambers.

When the reaction chamber is filled, the water is ejected through conduits, carrying the minerals, in a process as described in (Bassez 2019b §3.2). The reaction chamber discharges under the pressure of H_2 that is continuously generated and under the increase in heat that is released during the exothermic reactions. The minerals are deposited at the bottom of oceans as a function of their volumic mass, displaying gravitational sorting and the formation of horizontal layers. Oceans may not be required since the layers appear similar to those of the Lemptégy volcano deposited 30 000 years ago during the eruption of the neighboring Les Gouttes volcano, in France. The similarities will be the object of a next article. The reaction chambers fill and empty again in a process at the origin of the rythm in the layers. The widths of the meso- and macrobands depend on the sizes of the chemical
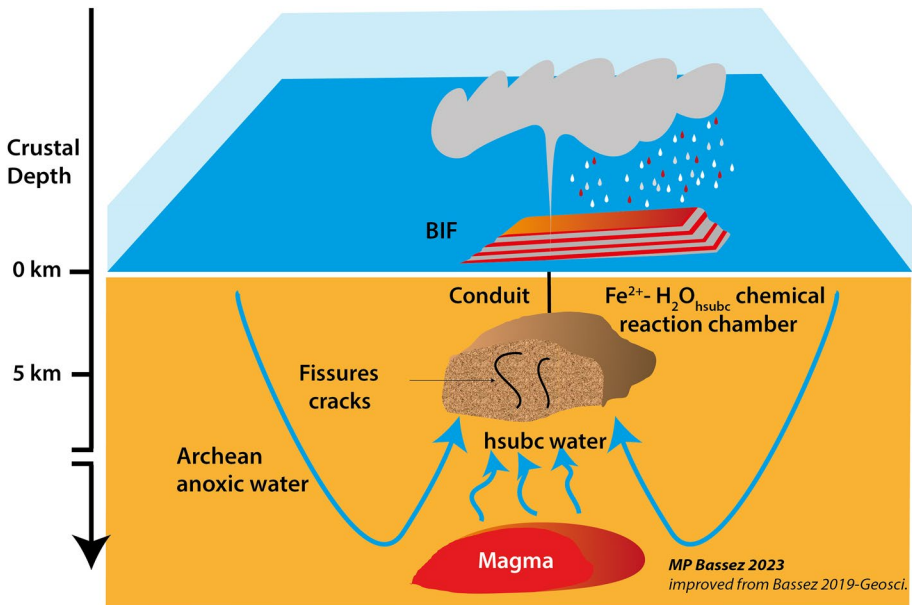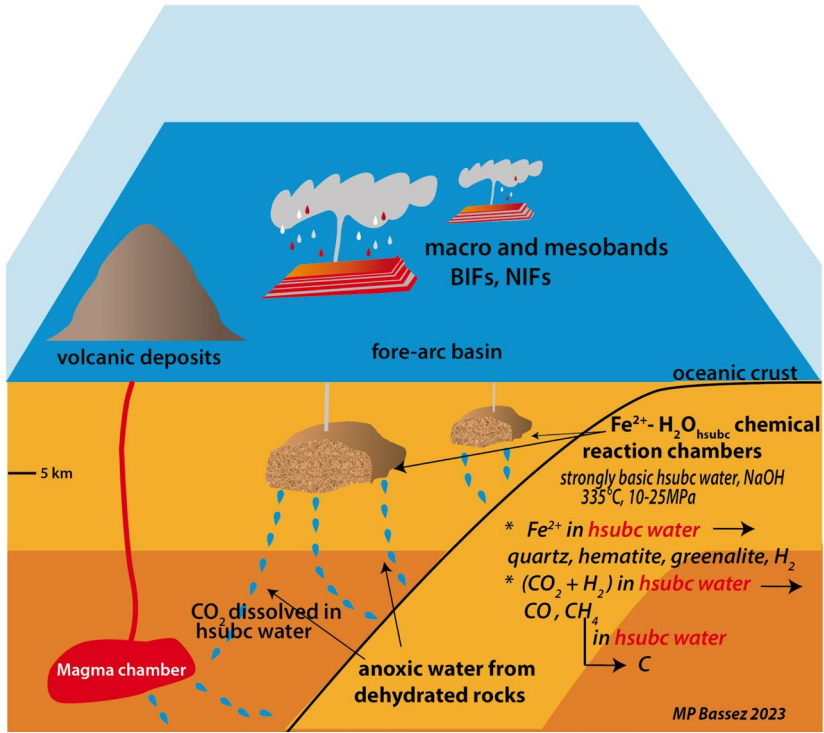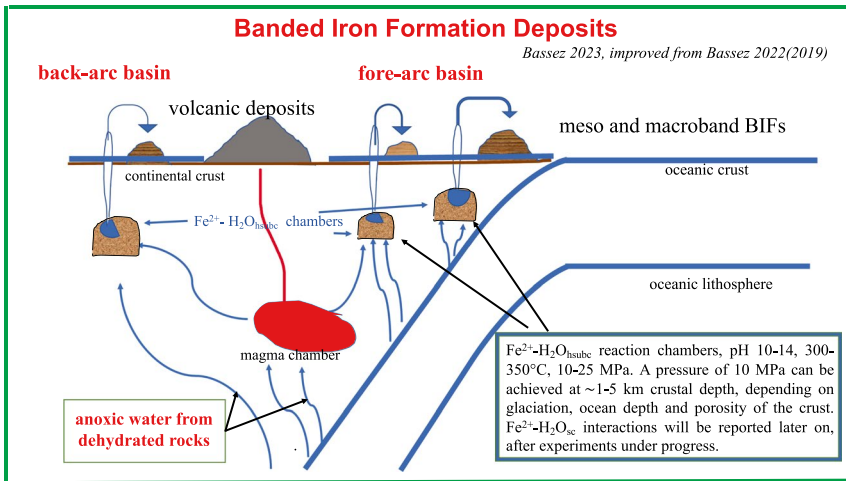

Fig. 17 Proposed geological construction of the Archean Banded Iron Formations

Fig. 18 Proposed geological construction of the banded iron formations during a subduction event in Archean times for BIFs, and in Neoproterozoic times for NIFs **a)** Hypothesis for the formation of BIFs and NIFs in fore-arc basins **b)** Hypothesis for the formation of BIFs and NIFs in fore-arc and back-arc basins. The diagram was presented at the f(O_2) international school on oxygen fugacity, Trieste, 5–9 September 2022

reaction chambers. Once the ferrous rocks are entirely transformed, the eruption ends. The great amount of quartz residing in the BIFs compared to the overlying basaltic rocks can be explained by the chemical reactions of Fig. 16, with quartz being a product of the two parallel reactions of formation of hematite and siderite.

The blocks of ferrous rocks can be positioned at a depth within ~5 km of the surface, where pressure corresponds to the high subcritical domain of water, as calculated in (Bassez 2019a, 2022 Fig. 2). Indeed, the depths of magma chambers, which are the sources of modern volcanism, have been shown to be approximately 11–15 km inside the Earth's crust (Becerril et al. 2013). Volcanoes that have erupted, may erupt again from magma chambers located at a higher level, nearer to the surface, than the first source. This is the case for the modern Usu volcano, which has been described with a source magma chamber at ~10 km. After the eruption, a new magma chamber formed at a depth of 4 km. *"Since then, beneath Usu volcano there have been two magma chambers, the deeper rhyolitic chamber and the shallower dacitic chamber. "* (Tomiya 2000). The blocks of ferrous rocks, such as fayalite and ferrosilite, may be positioned at depths where water is in the supercritical state. Experimental data will be obtained after completion of the hydrothermal and synchrotron experiments currently under preparation.

Figure 18 illustrates the case of BIF formation associated with subduction in Neoproterozoic times, and is improved from Fig. 2 in (Bassez 2022/2019). The subduction process hypothesis drawn for fore-arc basins can be extended to back-arc basins. During the subduction of an oceanic plate under a continental plate, at a certain depth, rocks dehydrate, releasing water without dissolved oxygen. Part of the released water contributes to the melting of some encountered rocks, creating magmas, and other parts continue to circulate. Before mixing with oxic meteoric water, the anoxic water can interact with ferrous rocks, leading to the minerals of Fig. 16. The geological process involving such subduction zones seems appropriate to explain the Egyptian Neoproterozoic Iron Formations, NIFs, ~850–700 Ma in age, a time when percolating meteoric water contained dissolved oxygen. The Central Eastern Desert of Egypt, CED, is part of the Arabian Nubian Shield, ANS, which is represented at ages of 825 Ma and 720 Ma in (Li et al. 2008 and Suppl) and which currently includes one tectonostratigraphic unit composed of *"arc-type volcanic/volcano sedimentary units along with…ophiolites"* (Hamimi et al. 2019 and refs therein). The CED is described as containing *"rocks with strong oceanic affinities"* (Stern and Hedge 1985 and refs therein). The term oceanic rock is often replaced by ophiolitic rock or ophiolitic mélange. They represent the rocks of an "*oceanic lithosphere that has been thrust onto a continental margin"* (di Pietro 2013). The NIFs of the CED are positioned within volcanic rocks: *"Neoproterozoic iron formations in Egypt…are interbedded with wackes, tuffs, lapilli and subordinate volcanic flows (basalts, andesites, dacites)"* (Gaucher et al. 2015 and refs therein). Basta et al. (2011) noticed *"a genetic relationship between volcanic activity and BIF"* at the Wadi Karim and Um Anab BIFs. El-Shazly and Khalil (20142016) and El-Shazly et al. (2019) proposed that the *"CED represents remnants of an island arc system formed above a southwest-dipping subduction zone"* and that Fe^{2+} was oxidized either by biota or photosynthesis during periods of arc quiescence. If anoxic alkaline hsubc water were interacting inside the CED Earth's crust or upper mantle with a block of fayalite, ferrosilite or ferrous rock, oxidation of ferrous iron could occur without the need for photosynthesis or microorganisms. Figure 18 represents an oceanic plate subducting under a continental plate, such as Arabia and Nubia. The Fe^{2+}-H_2O_{hsubc} chambers may be located ~1 to 5 km from the surface depending on glaciation, ocean depth and crustal porosity, or at further depths when the interaction proceeds in the supercritical state of

water. Mineral deposits may occur within shallow-water fore-arc or back-arc basins, creating parallel and horizontal layers.

The process of BIF formation associated with subduction can also be proposed for Archean BIFs. Bedrock lithologies mapped across the *"Makhonjwa Mountains, traditionally referred to as the Barberton Greenstone Belt"*, reveal *"signs of modern oceanic back-arc crust and subduction-related processes…* (which) *are similar to* (the) *terrains flanking Western Pacific-like subduction zones. Plate tectonics…were well established by 3.2–3.6 Ga"* (de Wit et al. 2018).

Figure 18 can be applied to BIFs of all ages, while the process of percolating anoxic meteoric water of Fig. 17 can be applied only to BIFs of Archean ages because meteoric water in Neoproterozoic times was oxygenated.

Conclusion

The present article reports Raman spectroscopic analyses of a segment located between 471.26 m and 471.48 m of the BARB3 drill core in the 3.4 Ga Buck Reef Chert. The results can be interpretated by the oxidation of ferrous silicates such as fayalite and ferrosilite by high subcritical water at strongly basic pH. Conclusions about the interaction with supercritical water will be produced after experiments in progress.

Data were obtained from four different Raman instruments located in Johannesburg, South Africa, and in CY Cergy Paris, Orléans and Lille, France. The wavenumber of the excitation laser was 532 nm. The studied segment of the BARB3 drill core consists of banded iron layers, which contain five unmetamorphosed minerals made of only five elements Fe, Si, O, C and H: quartz, hematite, siderite, ferrous-ferric greenalite and disordered graphite. The minerals can be considered as primary. They are observed in banded iron formations (BIFs). The observations confirm the presence of quartz and siderite as reported in (Bassez 2018). They provide unambiguous determinations of disordered graphitic carbon, hematite and no magnetite. Hematite and siderite are present in alternate layers in a quartz matrix. Two Raman peaks may indicate the presence of greenalite in the matrix of the quartz grain where the fluid inclusion has been studied. Only five fluid inclusions, 1 to 2 µm in size, have been recognized on the entire thin section. Liquid water, gaseous methane and sodium hydroxide, NaOH, at high concentration, 1:7 (1 mol NaOH per 7 mol water), are assigned in the two studied inclusions. A calculation concludes in pH 15, suggesting an Archean water which was strongly basic. Fe^{2+} oxidation could easily proceed. The phyllosilicate Fe^{III}-greenalite, $(Fe^{II}Fe^{III})_{3\text{-}2}Si_2O_5(OH)_4$, may also be present inside the inclusions.

A comparison of Raman spectra recorded for the disordered graphitic carbon of the BARB3_23B drilled BIF with those reported by other authors for various samples shows that the Raman profiles of the BARB3_23B resemble the carbon matter observed in the group of Archean cherts 3.5 Ga to 2.7 Ga in age, and more specifically those of the four stratigraphic levels from 3.48 Ga to 3.26 Ga, which were reported in (Hofmann et al. 2013a) for outcropping samples of the Komati, Hooggenoeg (including Buck Reef), Kromberg and Mendon Formations of the Onverwacht Group in the Barberton greenstone belt. The outcropping samples display disordered carbon with grain sizes ten times larger, and greater amounts of minerals that were optically identified. The BARB3_23B carbon

matter has been submitted to temperatures of ~335 °C, which is the domain of temperature of high subcritical water required for the anoxic strongly basic oxidation of ferrous iron to proceed. Very low amounts of oxygen and no hydroxyl functional groups compose its graphitic structure. It resembles the carbon matter of the CV_{oxA} Allende-like chondrites which contains minor phyllosilicates, no fayalite and no magnetite.

The origin of the methane is proposed as follows: when Archean CO_2-rich water containing no dissolved O_2 percolates inside the Earth crust and encounters blocks of ferrous minerals at temperatures and pressures of the high subcritical water and at high pH, the CO_2 can locally react with the H_2 produced during the oxidation of Fe^{2+} and transform into CO and CH_4. This proposition is based on laboratory experiments conducted by other authors who show the physico-chemical conditions for the transformation of CO_2 into CO and then CH_4. The CH_4-rich fluid can thus form in the proximity of ferrous minerals that are under the process of oxidation. The origin of the disordered graphitic carbon is proposed as a deposition from this anoxic methane-rich fluid. The conclusion is drawn following the study of the 1984 Holloway's C-O–H thermodynamic diagrams and experimental works on methane cracking.

Molecules of life may plausibly form inside the 3.4 Ga BARB3_23B quartz (or siderite) fluid inclusions which are cavities without membranes or with a fictitious membrane made of quartz with silicon and oxygen atoms. In these thermodynamic closed systems, chemical reactions may occur at equilibrium without exchange of matter with the mineral. Water and its concentrated dissolved components Fe^{2+} and SiO_2 can lead to Fe^{III}-greenalite. Specific orientations of the chemical bonds can occur at the surface of the cavity, leading to possible chiral molecules.

The alternate path of ferrous iron oxidation which involves anoxic strongly basic high subcritical water can explain the formation of Precambrian ferric minerals inside the Earth's crust during subduction events or not. Conclusions about the Fe^{2+} oxidation by supercritical water will be reported later on. Hypotheses for the formation of Archean and Neoproterozoic banded iron formations are presented in the present article on two figures improved from earlier drawings and a newly drawn third figure which emphasizes the various roles of high subcritical water. It does not exclude the currently accepted hypotheses which consider either surface UV light or microorganisms. However, it has the advantage of considering the structure of crustal water and the possible formation inside quartz cavities, of molecules of life that are required for life to emerge.

The theoretical model (Bassez 2013) which involves anoxic strongly basic water in its high subcritical domain of temperature, pressure and density, is spectroscopically confirmed in the present article with the observations of the minerals, the NaOH solution at pH 15, and the methane and disordered graphitic carbon, inside 3.4 Ga ferruginous banded layers. Further experiments are in preparation. Observations at the nanometer scale of the BARB3_23B with AFM-IR (Dazzi et al. 2004; Dazzi and Deniset-Besseau 2019) will indicate if the quartz cavities (fluid inclusions) contain organic matter. A microthermometry study of the inclusions would help obtaining knowledge on the temperature of homogenization and on the density of the H_2O-NaOH fluid (Pêcher and Boullier 1984; Cousseran et al. 1998; Dubois 2019). Confirmation of the alternate path of oxidation of ferrous iron, of the plausible synthesis of molecules of life inside quartz or siderite cavities, and of the construction of BIFs are experimentally envisioned. For instance, the study of the isotopic composition of oxygen in hematite, and of carbon in siderite, methane and disordered graphitic carbon would specify the origins of their formation. HRTEM images of the disordered graphitic carbon in the BARB3_23B can be compared with other carbon samples for conclusion on a plausible transition in the structure of geological carbon matter at the

time of the Great Oxidation Event. The oxidation of ferrous iron in anoxic alkaline high subcritical water and supercritical water, conducted in experiments avoiding O_2 contamination and analyzed either with Mössbauer or XANES spectroscopy would confirm the alternate path of Fe^{2+} oxidation, without O_2, UV light, or microorganisms. The oxidation must be conducted above the critical point of water because there is a lack of experiments in this domain, and the E-pH diagrams, which are the basis of the proposed alternate path of oxidation, cannot currently be drawn for the supercritical state of water. Experimental knowledge of the alkaline anoxic oxidation of ferrous iron by supercritical water may contribute to explain the formation of ferric iron minerals in the deeper crust and the upper mantle, where a great amount of Fe^{III} seems present under the form of Fe_2O_3, inside the spinel baring peridotite. The spinel region constitutes about 2% of the mantle (Frost 2022). Such experiments would show the importance of considering the structure of water (Bassez 1998, 2003) and the possible continuity from rocks to molecules of life (Bassez 2003) through the process of Geobiotropy (Bassez 2016) which represents the transformation from the world of rocks to the world of life. They would help the understanding of many processes on Earth and in the Universe.

Le message de la découverte est dans la persévérance
Marie-Paule Bassez

Data Availability Not applicable.

Declarations

Ethics Approval Not applicable.

Consent to Publish Open Access; This article is licensed under a Creative Commons Attribution 4.0 International License, which permits use, sharing, adaptation, distribution and reproduction in any medium or format, as long as you give appropriate credit to the original author(s) and the source, provide a link to the Creative Commons licence, and indicate if changes were made. The images or other third party material in this article are included in the article's Creative Commons licence, unless indicated otherwise in a credit line to the material. If material is not included in the article's Creative Commons licence and your intended use is not permitted by statutory regulation or exceeds the permitted use, you will need to obtain permission directly from the copyright holder. To view a copy of this licence, visit http://creativecommons.org/licenses/by/4.0/. ReprintsandPermissions

Conflicts of Interest The authors declare no competing interests.

Open Access This article is licensed under a Creative Commons Attribution 4.0 International License, which permits use, sharing, adaptation, distribution and reproduction in any medium or format, as long as you give appropriate credit to the original author(s) and the source, provide a link to the Creative Commons licence, and indicate if changes were made. The images or other third party material in this article are included in the article's Creative Commons licence, unless indicated otherwise in a credit line to the material. If material is not included in the article's Creative Commons licence and your intended use is not permitted by statutory regulation or exceeds the permitted use, you will need to obtain permission directly from the copyright holder. To view a copy of this licence, visit http://creativecommons.org/licenses/by/4.0/.

References

Agangi A, Hofmann A, Elburg MA (2018) A review of Palaeoarchaean felsic volcanism in the eastern Kaapvaal craton: Linking plutonic and volcanic records. Geoscience Frontiers 9:667–688. https://doi.org/10.1016/j.gsf.2017.08.003

Alard O (2022) Personal communication at the f(O$_2$) international school, University of Trieste, Italia, September 05–09

Arndt NT, Wilson A, Hofmann A, Mason P, Lowe D, Tice M, Byerly G, Chunnett G (2012) Peering into the Cradle of Life: Scientific Drilling in the Barberton Greenstone Belt. Scientific Drilling 13:71. https://doi.org/10.5194/sd-13-65-2012open

Barrenechea JF, Luque FJ, Millward D, Ortega L, Beyssac O, Rodas M (2009) Graphite morphologies from the Borrowdale deposit (NW England, UK): Raman and SIMS data. Contrib Mineral Petrol 158(1):37–51. https://doi.org/10.1007/s00410-008-0369-y

Bassez MP (1998) Director of T Witzel report (1997-1998): "Test of a Molecular Geometry Software and Study of Supercritical Water". Institut Universitaire de Technologie, Université Robert Schuman, Strasbourg, France

Bassez MP (2003) Is high-pressure water the cradle of life? J Phys Condens Matter 15(24):L353–L361. https://doi.org/10.1088/0953-8984/15/24/101

Bassez MP (2009) (2008a) Synthèse prébiotique dans les conditions hydrothermales. Comptes Rendus. Chimie 12(6–7):801–807. https://doi.org/10.1016/j.crci.2008.10.013

Bassez MP (2008b) Synthèse prébiotique dans les conditions hydrothermales. Correction from the editor (article classified as full paper). Comptes Rendus. Chimie (2013):1071. https://doi.org/10.1016/j.crci.2008.10.014

Bassez MP (2009) Prebiotic synthesis under hydrothermal conditions. Orig Life Evol Biosph 39(3–4): 223–225. https://doi.org/10.1007/s11084-009-9164-7

Bassez MP (2013) Geochemical origin of biological molecules. Geophysical Research Abstracts Vol 15, EGU2013–22. EGU'2013:Vienna, Austria, Session: Planetary & Solar System Sciences, Origins and Astrobiology, Planetary Evolution and Life, PS8.1, Oral: Tues. April 09–9h30. http://meetingorganizer.copernicus.org/EGU2013/EGU2013-22.pdf

Bassez MP (2015) Water, air, earth and cosmic radiation. Orig Life Evol Biosph 45(1–2):5–13. https://doi.org/10.1007/s11084-015-9402-0

Bassez MP (2016) Geobiotropy. LPSC'2016, The Woodlands, US. Abstr #1853. http://www.hou.usra.edu/meetings/lpsc2016/pdf/1853.pdf

Bassez MP (2017a) Ferromagnesian silicate and ferrosulfide rocks as a source of magnetite and hydrogen. Procedia Earth and Planetary Science 17: 492–495. 15th Water-Rock Interaction International Symposium, WRI-15, Evora, 16–21 Oct. 2016. https://doi.org/10.1016/j.proeps.2016.12.124

Bassez MP (2017) Anoxic and oxic oxidation of rocks containing Fe(II)Mg-silicates and Fe(II)-monosulfides as a source of Fe(III)-minerals and hydrogen. Geobiotropy. Orig Life Evol Biosph 47(4):453–480. https://doi.org/10.1007/s11084-017-9534-5

Bassez MP (2017c) Fluid Inclusions in Radioactive Rocks and Geobiotropy. European Current Research on Fluid Inclusions, ECROFI'2017c, Nancy France 23–29 June. Session : New Frontiers in inclusion research. Poster #S2.P02. http://2017c.ecrofi.univ-lorraine.fr/files/2016/03/catalogue-ecrofi-basseresolution2.pdf

Bassez MP (2018) Water near its supercritical point and at alkaline pH for the production of ferric oxides and silicates in anoxic conditions. A new hypothesis for the synthesis of minerals observed in banded iron formations and for the related geobiotropic chemistry inside fluid inclusions. Origins of Life and Evolution of Biospheres 48(3):289–320. https://doi.org/10.1007/s11084-018-9560-y

Bassez MP (2019a) Follow the high subcritical water. Geosciences 9(6):249(25pp). https://doi.org/10.3390/geosciences9060249

Bassez MP (2019b) High subcritical water-rock interaction for the formation of ferric minerals, in the absence of oxygen, UV light and microorganisms. E3S Web of Conferences 98: 01002 (6pp) WRI-16. https://doi.org/10.1051/e3sconf/20199801002

Bassez MP (2022/2019) Can the high subcritical water contribute to explain the Neoproterozoic BIFs? In: Cinner A et al. (eds) Recent Research on Geomorphology, Sedimentology, Marine Geosciences and Geochemistry, ASTI-Springer pp 289–291. Proceedings of the 2nd Springer conference CAJG (2019). https://doi.org/10.1007/978-3-030-72547-1_62

Bassez MP, Takano Y, Okhouchi N (2009) Organic analysis of peridotite rocks from the Ashadze and Logatchev hydrothermal sites. Int J Mol Sci 10:2986–2998. https://doi.org/10.3390/ijms10072986

Bassez MP, Takano Y, Kobayashi K (2012) Prebiotic organic microstructures. Orig Life Evol Biosph 42:307–316. https://doi.org/10.1007/s11084-012-9290-5

Basta FF, Maurice AE, Fontboté L, Favarger PY (2011) Petrology and geochemistry of the banded iron formation (BIF) of Wadi Karim and Um Anab, Eastern Desert, Egypt: implications for the origin of Neoproterozoic BIF. Precambrian Res 187:277–292. https://doi.org/10.1016/j.precamres.2011.03.011

Baumgartner M, Bakker RJ (2009) Raman spectroscopy of pure H_2O and $NaCl$-H_2O containing synthetic fluid inclusions in quartz–a study of polarization effects. Mineral Petrol 95:1–15. https://doi.org/10.1007/s00710-008-0028-z

Becerril L, Galindo I, Gudmundsson A, Morales JM (2013) Depth of origin of magma in eruptions. Sci Rep 3:2762. https://doi.org/10.1038/srep02762

Beyssac O, Lazzeri M (2012) Application of Raman spectroscopy to the study of graphitic carbons in the Earth Sciences. In: Dubessy J, Caumon MC, Rull F (eds) Raman spectroscopy applied to Earth Sciences and cultural heritage, EMU Notes in Mineralogy, vol 12, chp 12, pp 415–454. https://doi.org/10.1180/EMU-notes.12.12

Bonal L, Quirico E, Flandinet L, Montagnac G (2016) Thermal history of type 3 chondrites from the Antarctic meteorite collection determined by Raman spectroscopy of their polyaromatic carbonaceous matter. Geochim Cosmochim Acta 189:312–337. https://doi.org/10.1016/j.gca.2016.06.017

Bourbin M, Derenne S, Gourier D, Rouzaud JN, Gautret P, Westall F (2012) Electron Paramagnetic Resonance study of a photosynthetic microbial mat and comparison with Archean cherts. Orig Life Evol Biosph 42:569–585. https://doi.org/10.1007/s11084-012-9320-3

Bourdelle F, Benzerara K, Beyssac O, Cosmidis J, Neuville DR, Brown GE, Paineau E (2013) Quantification of the ferric/ferrous iron ratio in silicates by scanning transmission X-ray microscopy at the Fe $L_{2,3}$ edges. Contrib Mineral Petrol 166(2):423–434. https://doi.org/10.1007/s00410-013-0883-4

Buseck PR, Beyssac O (2014) From organic matter to graphite: Graphitization. Elements 10:421–426. https://doi.org/10.2113/gselements.10.6.421

Cairns-Smith, (1978) Precambrian solution photochemistry, inverse segregation, and banded iron formations. Nature 276:807–808

Carey D (1996) Measurements of the Raman spectrum of liquid water. Report KAPL-P-000226 USA.

Carey DM, Korenowski GM (1998) The measurement of the Raman spectrum of liquid water. J Chem Phys 108(7):2669–2675. https://doi.org/10.1063/1.475659

Carrière C (2017) Influence de la corrosion du fer sur les processus d'altération du verre: approche analytique multi-échelle. Thèse de doctorat, Université Pierre et Marie Curie, Paris VI, NNT: 2017PA066299

Catling DC, Zahnle K (2020) The Archean atmosphere. Sci Adv 6:eaax1420

Chen CS, Cheng WH, Lin SS (2000) Mechanism of CO formation in reverse water-gas shift reaction over Cu/Al_2O_3 catalyst. Catalysis Lett 68:45–48

Chinnasami SS, Mishra B (2017) Genetic implications of fluid-deposited disordered graphite and methane-rich inclusions in the Jonnagiri granodiorite-hosted gold deposit, Eastern Dharwar Craton, India. Ore Geol Rev 89:587–593. https://doi.org/10.1016/j.oregeorev.2017.07.006

Cook WG, Olive RP (2012) Pourbaix diagrams for the iron-water system extended to high- and low-supercritical conditions. Corros Sci 55:326–331. https://doi.org/10.1016/j.corsci.2011.10.034

Corridoni T, Sodo A, Bruni F, Ricci MA, Nardone M (2007) Probing water dynamics with OH^-. Chem Phys 336(2–3):183–187. https://doi.org/10.1016/j.chemphys.2007.06.013

Cousseran S, Pêcher A, Bintz P (1998) Application de l'étude des inclusions fluides aux quartz taillés de quelques sites préhistoriques dans les Alpes du Nord. Revue d'Archéométrie 22:103–109. https://doi.org/10.3406/arsci.1998.966

Dazzi A, Deniset-Besseau A (2019) AFM-IR: caractérisation chimique à l'échelle nanométrique. Techniques de l'ingénieur IN224 V1: 1–13 and Doc IN224: 1–3

Dazzi A, Prater CB, Hu Q, Chase DB, Rabolt JF, Marcott C (2004) AFM-IR; Combining Atomic Force Microscopy and Infrared Spectroscopy for nanoscale chemical characterization. Applied Spectroscopy 66(12):1365–1384

de Faria DLA, Lopes FN (2007) Heated goethite and natural hematite: Can Raman spectroscopy be used to differentiate them? Vibrational spectroscopy 45:117–121. https://doi.org/10.1016/j.vibspec.2007.07.003

de Oliveira DM, Bredt AJ, Miller TC, Corcelli SA, Ben-Amotz D (2021) Spectroscopic and structural characterization of water-shared ion-pairs in aqueous sodium and lithium hydroxide. J Phys Chem B 125:1439–1446. https://doi.org/10.1021/acs.jpcb.0c10564

de Vries ST, Nijman W, Armstrong RA (2006) Growth-fault structure and stratigraphic architecture of the Buck Ridge volcano-sedimentary complex, upper Hooggenoeg Formation, Barberton Greenstone Belt, Sth Africa. Precambrian Res 149:77–98. https://doi.org/10.1016/j.precamres.2006.04.005

de Wit M, Furnes H, MacLennan S, Doucouré M, Schoene B, Weckmann U, Martinez U, Bowring S (2018) Paleoarchean bedrock lithologies across the Makhonjwa Mountains of South Africa and Swaziland linked to geochemical, magnetic and tectonic data reveal early plate tectonic genes flanking subduction margins. Geosci Front 9:603–665. https://doi.org/10.1016/j.gsf.2017.10.005

de Wit MJ, Furnes H, Robins B (2011) Geology and tectonostratigraphy of the Onverwacht Suite, Barberton Greenstone Belt, South Africa. Precambrian Res 186:1–27. https://doi.org/10.1016/j.precamres.2010.12.007

Delarue F, Rouzaud JN, Derenne S, Bourbin M, Westall F, Kremer B, Sugitani K, Deldicque D, Robert F (2016) The Raman-derived carbonization continuum: a tool to select the best preserved molecular structures in Archean kerogens. Astrobiology 16(6):1–11. https://doi.org/10.1089/ast.2015.1392

di Pietro JA (2013) Landscape Evolution in the United States, Chapter 20, Keys to the interpretation of geological history: Ophiolite, subduction complexes, and collision. p 339. https://doi.org/10.1016/B978-0-12-397799-1.00020-8

Dubois M, Monnin C, Castelain T, Coquinot Y, Gouy S, Gauthier A, Goffé B (2010) Investigation of the H_2O-NaCl-LiCl system: a synthetic fluid inclusion study and thermodynamic modeling from -50° to +100°C and up to 12 mol/kg. Econ Geol 105:329–338. https://doi.org/10.2113/gsecongeo.105.2.329

Dubois M (2019) The world of fluid inclusions. https://fluid-inclusions.univ-lille.fr/co/008_homogenization_critical_phase.html

El-Shazly AK, Khalil KI (2014) Banded iron formations of Um Nar, Eastern Desert of Egypt: P-T-X conditions of metamorphism and tectonic implications. Lithos 196–197:356–375. https://doi.org/10.1016/j.lithos.2014.01.006

El-Shazly AK, Khalil KI (2016) Metamorphic and geochronologic constraints on the tectonic evolution of the Central Eastern Desert of Egypt. Precambrian Res 283:144–168. https://doi.org/10.1016/j.precamres.2016.07.016

El-Shazly AK, Khalil KI, Helba HA (2019) Geochemistry of banded iron formations and their host rocks from the Central Eastern Desert of Egypt: a working genetic model and tectonic implications. Precambrian Res 325:192–216. https://doi.org/10.1016/j.precamres.2019.02.011

Foucher F, Guimbretière G, Bost N, Westall F (2017) Petrographical and mineralogical applications of Raman mapping. In: Maaz K (ed) Raman Spectroscopy and Applications, IntechOpen, Chapter 8, pp.163–180. https://doi.org/10.5772/65112

French BM, Rosenberg PE (1965) Siderite ($FeCO_3$): Thermal decomposition in equilibrium with graphite. Science 147:1283–1284. https://doi.org/10.1126/science.147.3663.1283

Frezzotti ML, Tecce F, Casagli A (2012) Raman spectroscopy of fluid inclusion analysis. J Geochem Explor 112:1–20. https://doi.org/10.1016/j.gexplo.2011.09.009

Frost D (2022) Oxidation state of the Earth from the core to the mantle transition zone. Oral presentation at the f(O$_2$) International School, Trieste, Italy, 09 September

Fu Q, Seyfried WE Jr (2009) Experimental study of abiotic synthesis processes in a hydrothermal flow system: implications for organic matter formation in extraterrestrial environments. Abstract 2504.pdf-40th Lunar Planetary Sci Conf

Fu X, Wang A, Krawczynski JM (2017) Characterizing amorphous silicates in extraterrestrial materials: Polymerization effects on Raman and mid-IR spectral features of alkali and alkali earth silicate glasses. J Geophys Res Planets 122:839–855. https://doi.org/10.1002/2016JE005241

Gaucher C, Sial AN, Frei R (2015) Chemostratigraphy of Neoproterozoic banded iron formation (BIF): types, age and origin. Chap. 17, p. 433–449 Chemostratigraphy. M Ramkuar ed. Periyar University, Salem, Tamilnadu, In. https://doi.org/10.1016/B978-0-12-419968-2.00017-0

Ghosh N, Roy S, Bandyopadhyay A, Mondal JA (2023) Vibrational Raman spectroscopy of the hydration shell of ions. Liquids 3:19–39. https://doi.org/10.3390/loquids3010003

Guggenheim S, Bailey SW, Eggleton RA, Wilkes P (1982) Structural aspects of greenalite and related minerals. The Canadian Mineralogist 20:1–18

Guggenheim S, Eggleton RA (1998) Modulated crystal structures of greenalite and caryopilite: a system with long-range, in-plane structural disorder in the tetrahedral sheet. Can Mineral 36:163–179

Hamimi Z, Abd El-Wahed MA, Gahlan HA, Kamh SZ (2019) Tectonics of the Eastern Desert of Egypt: key to understanding the Neoproterozoic evolution of the Arabian-Nubian Shield (East African Orogen). In: Bendaoud A et al. (eds) The Geology of the Arab World-an Overview, Springer Geology, pp 1–81. https://doi.org/10.1007/978-3-319-96794-3_1

Hill HGM, Nuth J (2003) The catalytic potential of cosmic dust: implications for prebiotic chemistry in the solar nebula and other protoplanetary systems. Astrobiology 3(2):291–304

Hinz I (2018) Understanding abiotic and biotic mechanisms associated with the formation of iron-silicates like low Fe(III) greenalite in banded iron formations. Ph.D. thesis, Univ. Colorado, Boulder

Hofmann A, Bolhar R, Orberger B, Foucher F (2013) Cherts of the Barberton Greenstone Belt, South Africa: petrology and trace-element geochemistry of the 3.5 to 3.3 Ga old silicified volcaniclastic sediments. S Afr J Geol 116(2):297–322. https://doi.org/10.2113/gssajg.116.2.297

Hofmann A, Karykowski B, Mason P, Chunnet G, Arndt N (2013b) Barberton drilling project-Buck Reef Chert core BARB3. Geophys Res Abs 15:EGU2013b–12227

Holloway JR (1984) Graphite-CH4-H2O-CO2 equilibria at low-grade metamorphic conditions. Geology 12:455–458

Horvath E, Kristof J, Frost RL (2010) Vibrational spectroscopy of intercalated kaolinites. Part-I. Appl Spectrosc Rev 45:130–147. https://doi.org/10.1080/05704920903435862

ICDP (2011) General view of Buck Reef. Image UN_5047_2_A_drillsite_3.jpg. http://barberton.icdp-online.org/

Johnson JE, Muhling JR, Cosmidis J, Rasmussen B, Templeton AS (2018) Low-Fe(III) greenalite was a primary mineral from Neoarchean oceans. Geophys Res Lett 45. https://doi.org/10.1002/2017GL076311

Kiyokawa S, Suzuki T, El-Dokouny HA, Dawoud M, Abuelhasan MM (2020) Stratigraphy, petrology, and geochemistry of a neoproterozoic banded iron sequence in the El-Dabbah Group, central Eastern Desert, Egypt. J Afr Earth Sci 168:103805. https://doi.org/10.1016/j.jafrearsci.2020.103805

Klein C Jr (1974) Greenalite, stilpnomelane, minnesotaite, crocidolite and carbonates in a very low-grade metamorphic Precambrian iron-formation. The Canadian Mineralogist 12:475–498

Klein C, Bricker OP (1977) Some aspects of the sedimentary and diagenetic environment of Proterozoic Banded Iron Formations. Economic Geology 72:1457–1470

Kröner (Krüner) A, GR Byerly, DR Lowe, (1991) Chronology of early Archaean granite greenstone evolution in the Barberton Mountain Land, South Africa, based on precise dating by single zircon evaporation. Earth and Planetary Science Letters 103:41–54

Lacroix B, Travé A, Buatier M, Labaume P, Vennemann T, Dubois M (2014) Syntectonic fluid-flow along thrust faults: example of the south-Pyrenean fold-and-thrust belt. Marine Petrol Geol 49:84–98. https://doi.org/10.1016/j.marpetgeo.2013.09.005

Ledevin M, Arndt N, Chauvel C, Jaillard E, Simionovici A (2019) The sedimentary origin of black and white Banded Cherts of the Buck Reef, Barberton. South Africa. Geosciences 9:424. https://doi.org/10.3390/geosciences9100424

Lepland A, van Zuilen MA, Philippot P (2011) Fluid-deposited graphite and its geobiological implications in early Archean gneiss from Akilia, Greenland. Geobiology 9:2–9. https://doi.org/10.1111/j.1472-4669.2010.00261.x

Lepot K, Addad A, Knoll AH, Wang J, Troadec D, Béché A, Javaux EJ (2017) Iron minerals within specific microfossil morphospecies of the 1.88 Ga Gunflint Formation. Nat Commun 8:14890. https://doi.org/10.1038/ncomms14890

Li L, Zhang X, Luan Z, Du Z, Xi S, Wang B, Lian C, Yan J (2018) A new approach to measuring the temperature of fluids reaching 300°C and 2 mol/kg NaCl based on the Raman shift of water. Appl Spectrosc 72(11):1621–1631. https://doi.org/10.1177/0003702818776662

Li ZX, Bogdanova SV, Collins AS, Davidson A, de Waele B, Ernst RE, Fitzsimons ICW, Fuck RA, Gladkochub DP, Jacobs J, Karlstrom KE, Lu S, Natapov LM, Pease V, Pisarevsky SA, Thrane K, Vernikovsky V (2008) Assembly, configuration, and break-up history of Rodinia: a synthesis. Precambrian Res 160:179–210. https://doi.org/10.1016/j.precamres.2007.04.021

Lowe DR, Byerly GR (1999) Stratigraphy of the west-central part of the Barberton Greenstone Belt, South Africa. In: Geological Evolution of the Barberton Greenstone Belt, South Africa. Lowe DR, Byerly GR (eds) The Geological Society of America, special paper 329, pp 1–36. https://doi.org/10.1130/0-8137-2329-9.1

Lowe DR, Byerly GR (2020) The non-glacial and non-cratonic origin of an early Archean felsic volcaniclastic unit, Barberton Greenstone Belt, South Africa. Precambrian Res 341:105647

Luque FJ, Crespo-Feo E, Barrenechea JF, Ortega L (2012) Carbon isotopes of graphite: Implications on fluid history. Geosci Front 3(2):197–207

Luque FJ, Ortega L, Barrenechea JF, Millward D, Beyssac O, Huizenga JM (2009) Deposition of highly crystalline graphite from moderate-temperature fluids. Geology 37(3):275–278. https://doi.org/10.1130/G25284A.1

Luque FJ, Pasteris JD, Wopenka B, Rodas M, Barrenechea JF (1998) Natural fluid-deposited graphite: mineralogical characteristics and mechanisms of formation. Am J Sci 298:471–498

Maj K, Kocemba I (2018) Nanostructured forms of carbon deposit obtained during cracking of methane reaction over nanocrystalline iron catalysts. Adsorp Sci Technol 36(1–2):493–507. https://doi.org/10.1177/0263617417705471

Marshall PC, Edwards GMH, Jehlicka J (2010) Understanding the application of Raman spectroscopy to the detection of traces of life. Astrobiology 10(2):229–243. https://doi.org/10.1089/ast.2009.0344

Marty B, Zimmermann L, Pujol M, Burgess R, Philippot P (2013) Nitrogen isotopic composition and density of the Archean atmosphere. Science 342:101–104. https://doi.org/10.1126/science.1240971

McMillan P (1984a) Structural studies of silicate glasses and melts–-applications and limitations of Raman spectroscopy. Am Miner 69:622–644

McMillan P (1984b) A Raman spectroscopic study of glasses in the system $CaO-MgO-SiO_2$ Am Miner 69:645–659

Milesi V, Guyot F, Brunet F, Richard L, Recham N, Benedetti M, Dairou J, Prinzhofer A (2015) Formation of CO_2, H_2 and condensed carbon from siderite dissolution in the 200–300°C range and at 50 MPa. Geochimica et Cosmochimica Acta 154:201–211. https://doi.org/10.1016/j.gca.2015.01.015

Nan J, King HE, Delen G, Meier F, Weckhuysen BM, Guo Z, Peng X, Plümper O (2021) The nanogeochemistry of abiotic carbonaceous matter in serpentinites from the Yap Trench, western Pacific Ocean. Geology 49:330–334. https://doi.org/10.1130/G48153.1

Nasdala L, Smith DC, Kaindl R, Ziemann MA (2004) Raman spectroscopy: analytical perspectives in mineralogical research. In: A Beran, E. Libowitzky (eds) Spectroscopic methods in mineralogy. Eötvös Univ. Press, EMU Notes in Mineralogy, Vol. 6, chapter 7, pp 281–343. ISBN 963 463 6624.

Neal C, Stanger G (1983) Hydrogen generation from mantle source rocks in Oman. Earth Planet Sci Lett 66:315–320

Parnell J, Brolly C, Boyce AJ (2021) Mixed metamorphic and fluid graphite deposition in Palaeoproterozoic supracrustal rocks of the Lewisian Complex, NW Scotland. Terra Nova 33:541–550. https://doi.org/10.1111/ter.12546

Pasteris JD, Chou IM (1998) Fluid-deposited graphitic inclusions in quartz: Comparison between KTB (German Continental Deep Drilling) core samples and artificially reequilibrated natural inclusions. Geochimica Et Cosmo Acta 62(1):109–122

Pastorczak M, Kozanecki M, Ulanski J (2008) Raman Resonance Effect in Liquid Water. J Phys Chem A Lett 112:10705–10707. https://doi.org/10.1021/jp805369p

Pêcher A, Boullier AM (1984) Evolution à pression et température élevées d'inclusions fluides dans un quartz synthétique. Bull Minéral 107:2. https://doi.org/10.3406/bulmi.1984.7745

Pizzarello S (2012) Catalytic syntheses of amino acids and their significance for nebular and planetary chemistry. Meteorit Planet Sci 47(8):1291–1296. https://doi.org/10.1111/j.1945-5100.2012.01390.x

Rasmussen B, Krapez B, Muhling JR (2014) Hematite replacement of iron-bearing precursor sediments in the 3.46 by old Marble Bar Chert, Pilbara craton. Australia. GSA Bull 126(9/10):1245–1258. https://doi.org/10.1130/B31049.1

Rasmussen B, Krapez B, Muhling JR, Suvorova A (2015) Precipitation of iron silicate nanoparticles in early Precambrian oceans marks Earth's first iron age. Geology 43(4):303–306. https://doi.org/10.1130/G36309.1

Rasmussen B, Muhling JR, Suvorova A, Krapez B (2017) Greenalite precipitation linked to the deposition of banded iron formations downslope from a late Archean carbonate platform. Precambrian Res 290:49–62. https://doi.org/10.1016/j.precamres.2016.12.005

Rice SA, Sceats MG (1981) A random network model for water. J Phys Chem 85:1108–1119

Sabatier P, Senderens JB (1902) Hydrogénation directe des oxydes du carbone en présence de divers métaux divisés. Comptes Rendus Des Séances Hebdomadaires De L'académie Des Sciences 134:689–691

Sadezky A, Muckenhuber H, Grothe H, Niessner R, Pöschl U (2005) Raman microspectroscopy of soot and related carbonaceous materials: Spectral analysis and structural information. Carbon 43:1731–1742. https://doi.org/10.1016/j.carbon.2005.02.018

Schad M, Byrne JM, ThomasArrigo LK, KretzschmarR Konhauser KO, Kappler A (2022) Microbial Fe cycling in a simulated Precambrian ocean environment: Implications for secondary mineral (trans) formation and deposition during BIF genesis. Geochim Cosmochim Acta 331:165–191. https://doi.org/10.1016/j.gca.2022.05.016

Shaffer CD (1998) Quantification of hydroxide in aqueous solutions by Raman spectroscopy. US Dept of Energy Contract DE-AC11–93PN38195

Stefanski J, Schmidt C, Jahn S (2018) Aqueous sodium hydroxide (NaOH) solutions at high pressure and temperature: insights from in situ Raman spectroscopy and ab initio molecular dynamics simulations. Phys Chem Chem Phys 20:21629. https://doi.org/10.1039/c8cp00376a

Stern RJ, Hedge CE (1985) Geochronologic and isotopic constraints on late Precambrian crustal evolution in the Eastern Desert of Egypt. Am J Sci 285:95–127

Tice MM, Lowe DR (2006) The origin of carbonaceous matter in pre-3.0 Ga greenstone terrains: A review and new evidence from the 3.42 Ga Buck Reef Chert. Earth Sci Rev 76:259–300. https://doi.org/10.1016/j.earscirev.2006.03.003

Tomiya A (2000) Depth of magma chamber determined by experimental petrologic methods. Proceedings World Geothermal Congress Kyushu-Tohoku, Japan, 1855–1859

Tosca NJ, Guggenheim S, Pufahl PK (2016) An authigenic origin for Precambrian greenalite: Implications for iron formation and the chemistry of ancient seawater. Geol Soc Am Bull 128:511–530. https://doi.org/10.1130/B31339.1

Wang A, Freeman JJ, Jolliff BL (2015) Understanding the Raman spectral features of phyllosilicates. J Raman Spectrosc 46(10):829–845. https://doi.org/10.1002/jrs.4680

Wang C, Robbins LJ, Planavsky NJ, Beukes NJ, Patry LA, Lalonde SV, Lechte MA, Asael D, Reinhard CT, Zhang L, Konhauser KO (2023) Archean to early Paleoproterozoic iron formations document a transition in iron oxidation mechanisms. Geochim Cosmochim Acta 343:286–303. https://doi.org/10.1016/j.gca.2022.12.002